UNCLASSIFIED

AD NUMBER

AD817805

NEW LIMITATION CHANGE

TO

Approved for public release, distribution unlimited

FROM

Distribution authorized to U.S. Gov't. agencies and their contractors; Critical Technology; JUN 1967. Other requests shall be referred to Air Force Institute of Technology, Attn: AFIT-SE, Wright-Patterson AFB, OH 45433.

AUTHORITY

AFIT memo. 22 Jul 1971

THIS PAGE IS UNCLASSIFIED

AD817805

AIR FORCE INSTITUTE OF TECHNOLOGY

AIR UNIVERSITY
UNITED STATES AIR FORCE

SCHOOL OF ENGINEERING

WRIGHT-PATTERSON AIR FORCE BASE, OHIO

AFLC-WPAFB-SEP 65 611

WATER IMPACT LOADS

ON STRUCTURES

THESIS

GAM/MECH 67-1 Ralph N. Bingman

"This document is subject to special export controls and each transmittal to foreign government or foreign nationals may be made only with prior approval of Dean, School of Engineering, Air Force Institute of Technology (AFIT-SE), Wright-Patterson Air Force Base, Ohio 45433.

AFLC-WPAFB-JUL 67 35

GAM/MECH 67-1

WATER IMPACT LOADS

ON STRUCTURES

THESIS

Presented to the Faculty of the School of Engineering of

the Air Force Institute of Technology

Air University

in Partial Fulfillment of the

Requirements for the Degree of

Master of Science

By

Ralph N. Bingman

Graduate Aerospace-Mechanical Engineering

May 1967

"This document is subject to special export controls and each transmittal to foreign government or foreign nationals may be made only with prior approval of Dean, School of Engineering, Air Force Institute of Technology (AFIT-SE), Wright-Patterson Air Force Base, Ohio 45433.

Preface

An important research goal in aerospace engineering is to provide greater accuracy in methods for predicting the dynamic force-time relationships that are associated with the critical design conditions of a modern flight vehicle. Improvements in the prediction of these dynamic forces enable an engineer to utilize new lightweight structures more effectively and to develop a more optimum structural design. The need for greater accuracy has continued to grow as new or more severe loading environments have been encountered and as modern flight vehicles have become more flexible.

In some of the more critical dynamic problem areas, such as problems in aeroelasticity, the flexibility of the structure has long been recognized as a governing parameter in the theoretical prediction of force distributions and force-time histories. However, in some other areas research has been sporadic, depending on particular requirements, and adequate, generalized theories have not been developed to account for the effects of structural flexibility. This is particularly true in the prediction of water-entry impact loads. Theories which were developed prior to World War II are still used; these theories cannot accommodate structural flexibility. The inherent flexibility of advanced aerospace structures can cause significant increases in the dynamic loads during water impact which are not accounted for using the available theoretical prediction methods.

This study has attempted to extend one of the most commonly used theories for determining water impact loads to include the coupled interactions of hydrodynamic, inertial and elastic forces. Many of the past theoretical and experimental investigations of water impact loads, including recent modeling programs by the NASA in developing the Mercury and Apollo spacecraft, have been conducted on bodies with spherical lower surfaces. This study has been limited to simple spherically shaped elastic structures. Also, the study has been limited to vertical flight paths into the water (no oblique landings).

I am deeply indebted to my thesis advisor, Dr. D. W. Breuer, Head of the Department of Mechanics at the Air Force Institute of Technology, for his patience and technical guidance throughout the course of this study. I would like to express my sincere appreciation to the members of my thesis committee, Dr. J. S. Przemieniecki, Assistant Dean for Research and Dr. P. J. Torvik, Associate Professor of Mechanics at the Air Force Institute of Technology for their counsel and suggestions. I also wish to thank Walter J. Mykytow, Assistant for Research and Technology, Charles E. Thomas, Chief of the Field Measurements Group and Virgil C. McIntosh, Field Measurements Group, all from the Vehicle Dynamics Division, Air Force Flight Dynamics Laboratory for their assistance during the background investigation and experimental portion of this study.

Ralph N. Bingman

Contents

	Page
Preface	ii
List of Figures	vi
List of Tables	viii
List of Symbols	ix
Abstract	xi
I. Introduction	1
Background	1
Purpose and Scope	4
II. Theoretical Development	5
Rigid Body Entering Water	5
Flexible Body Entering Water	15
Spring Stiffness for Shallow Spherical Shell	20
Solution of Differential Equations by the Runge-Kutta Method	32
III. Experimental Apparatus and Procedure	42
Model Design and Instrumentation	42
Water Impact Test Set-Up	45
Description of Acceleration Measuring Equipment	46
Test Procedure	46
IV. Experimental Results and Discussion	52
Data Reduction Procedure	52
Model Natural Frequencies of Vibration	57
Measured Impact Accelerations	58
Lower Shell Accelerations	58
Center of Gravity Accelerations	59
Rigid Body Type Accelerations	60
V. Comparison of Theoretical and Experimental Results	61
Comparison of Response Frequencies	62
Comparison of Acceleration Levels	64
VI. Conclusions	70
VII. Recommendations	72

Contents

		Page
Bibliography		73
Appendix A:	Theoretical Data on Rigid Body Water Impact Loads	74
Appendix B:	Theoretical Data on Flexible Body Water Impact Loads	82
Appendix C:	Experimental Data on Flexible Body Water Impact Loads	92
Appendix D:	Instrumentation Characteristics	99
Vita		101

List of Figures

Figure		Page
1	Comparison of Model Tests and Theoretical Analysis	3
2	Geometry for Bodies Entering Water	5
3	Angle ϕ	10
4	Comparison of Acceleration-Time Histories Obtained from Model Test, Full-Scale Test, and Theoretical Investigation. (Flight Path, 90°; Contact Attitude, 0°)	12
5	Time Histories of Velocity and Displacement for a Rigid Body Entering Water	13
6	Time Histories of Acceleration and Pressure for a Rigid Body Entering Water	14
7	Flexible Shell Coordinates During Water Impact	16
8	Typical Pressure Pattern Growth	19
9	Shell Geometry	20
10	Shell Edge Support and Loading for Calculation of Deflections by Matrix Methods	27
11	Spring Stiffness for a Spherical Shell Entering Water	31
12	Comparison of Velocity-Time Histories for Rigid and Flexible Structures	35
13	Comparison of Acceleration-Time Histories for Rigid and Flexible Structures	36
14	Comparison of Deflection-Time Histories for a Spherical Shell Structure Obtained from Dynamic Loading and Quasi-Static Loading (No Vibration)	37
15	Theoretical Deflection-Time History for a Spherical Shell Structure with Damping	38
16	Model of Two Degree of Freedom System	39
17	Sketch of the Water Impact Test Set-Up	43
18	Experimental Water Impact Model	44

List of Figures

Figure		Page
19	Block Diagram of Test Instrumentation	47
20	Instrumentation for Water Impact Tests	48
21	Experimental Model Before and After Contact with Water During Drop Test	50
22	Data Reduction Procedure	55
23	Synthesized Complex Waveform	56
24	Comparison of Acceleration-Time Histories Obtained from Theoretical Investigation and Model Test (Data from Model with 0.050 Inch Thick Spherical Shell)	65
25	Comparison of Acceleration-Time Histories Obtained from Theoretical Investigation and Model Test (Data from Model with 0.080 Inch Thick Spherical Shell)	66
26	Comparison of Theoretical Acceleration-Time Histories and Experimental Results	68
27	Variations in Peak Accelerations Corresponding to Changes in Contact Velocity, V_o, Radius, R, and Weight, W, for a Rigid Sphere Entering Water.	79
28	Comparison of Theoretical Acceleration-Time Histories for Two Values of the Constant in the Expression for the Virtual Mass of Water.	81
29	Deflection Shapes for a Spherical Shell Segment. . . .	83
30	Comparison of Acceleration-Time Histories for a Rigid Sphere and a Thick Spherical Shell	90
31	Tracing of Acceleration Record for Model with 0.032 Inch Thick Shell	93
32	Tracing of Acceleration Record for Model with 0.050 Inch Thick Shell	94
33	Tracing of Acceleration Record for Model with 0.080 Inch Thick Shell	95

List of Tables

Table		Pages
I	Calculated Values of the Parameter μ	23
II	Data for the Evaluation of Shell Deflections	26
III	Deflections and Buckling Pressures for a Spherical Shell.	28
IV	Water Impact Model Test Conditions	51
V	Water Impact Model Natural Frequencies of Vibration	57
VI	Comparison of Coupled Structural-Water Frequencies of Vibration Obtained from Theoretical and Experimental Investigations.	63
VII	Rigid Body Water Impact Loads	75
VIII	Summary of Theoretical Data for Rigid Sphere Entering Water	78
IX	Runge-Kutta Solution for Differential Equations. . .	86
X	Comparison of Relative Deflections as Obtained from the Structural Inertia Force and the Hydrodynamic Reaction Force	89
XI	Experimental Results for Model with 0.032 Inch Thick Shell.	96
XII	Experimental Results for Model with 0.050 Inch Thick Shell.	97
XIII	Experimental Results for Model with 0.080 Inch Thick Shell.	98

List of Symbols

C	Constant in the ratio of virtual mass of water to structural mass
E	Percent error. Also, modulus of elasticity
F(i)	Variable in computer program
F,P	Force
K	Spring stiffness for a spherical shell
M	Mass of a structural body
R	Radius of a sphere. Also, a subscript for rigid structure
V_o	Velocity of a structural body at the moment of first contact with the water
W	Weight of a structural body
a	Radius of a flexible spherical shell
c	Horizontal radius of distributed loading on a spherical shell. Also, damping coefficient and velocity of sound in water
g	Acceleration due to gravity
h	Shell thickness
ℓ	Characteristic length in the analytical expression for the deflection of a spherical shell
m*	Virtual mass of water
p	Pressure
p_{cr}	Critical buckling pressure for a spherical shell
r	Dimension used in obtaining the instantaneous width of a body in the plane of the undisturbed water surface
s	Subscript for flexible structure
t	Time
y	Vertical penetration depth of a rigid body entering water

List of Symbols

y_1	Vertical displacement of the center of mass of a flexible body entering water
y_2	Vertical displacement of the lower center of a flexible body entering water
$y(i)$	Variable in computer program
Δ	Small increment in time, displacement, or velocity
α	Angle of inclination of the under surface of a wedge with respect to the horizontal
δ_o, w_o	Deflection at the lower center of a spherical shell
ζ	Damping ratio c/c_{cr}
θ	Angle from the center of a sphere to the edge of a segment
μ	Parameter in the analytical expression for the deflection of a spherical shell
ν	Poisson's ratio
ρ	Density of water
σ	Critical buckling stress in a spherical shell
ϕ	Angle from the vertical center line to the outer edge of the applied force on a sphere
χ	A fraction between 0 and 1.0
ψ_4'	Parameter in the analytical expression for the deflection of a spherical shell
	Derivative with respect to time

Abstract

Theoretical and experimental investigations were made of the dynamic response characteristics of a simple elastic structure subjected to water impact loading. The purpose was to determine the effects of structural flexibility on the resulting dynamic loads and to see if a simple approximate mathematical technique for predicting these loads could be developed. In the theoretical portion of the investigation, water impact acceleration-time histories were computed for rigid spheres of different radii. The rigid body theory was then modified by considering the flexibility of thin spherical shells. A simple equation was developed for approximating the effective spring stiffness of the shell. Theoretical acceleration-time histories, based on the modified theory, are presented. For the experimental portion of the investigation, six drop tests were conducted using a model which incorporated thin aluminum spherical shell segments on the lower surface. Shells of 24 inch radius and 0.032, 0.040, 0.050 and 0.080 inch thickness were tested. Qualitative agreement was obtained between results from the model tests and the modified theory. The theoretically predicted acceleration levels averaged 10 percent lower than the experimental values. However, quantitative comparisons of acceleration levels are limited because the experimental model had more degrees of freedom excited than the lowest one which was used in the approximate theory. Significant coupled vibratory responses of the shell and water were predicted by theory and were observed in the experimental results. The predicted vibration frequencies averaged 20 percent above the experimentally observed frequencies.

WATER IMPACT LOADS ON STRUCTURES

I. Introduction

Background

When recoverable missiles, manned reentry spacecraft, and various research vehicles land in water, severe dynamic loadings are imposed on the vehicle structure. Although recent advances in structural technology have enabled the development of efficient lightweight structures capable of operating in severe loading environments, these structures are generally elastic and deform under dynamic loadings. The motions and stresses in a flexible vehicle resulting from water impact involve very complex interactions of hydrodynamic, inertial, and elastic forces. Therefore, the design of a vehicle capable of withstanding water entry impact loads requires careful consideration of the dynamic interactions among these forces.

The published literature contains several theoretical approaches for predicting water impact loads. Past investigators have classified the water entry phenomenon into three phases based on certain physical relationships and mathematical treatments involved. These are the shock-wave phase, the flow line establishment phase, and the quasi-steady flow phase (with and without a cavity over the aft portion of the vehicle). Mosteller (Ref 1:2-8) and Collopy (Ref 2:77-86)have presented discussions of the various phases and the theories which have been developed for each phase.

The shock wave phase is of very short duration (on the order of 50 to 100 micro seconds) and occurs while the line of contact between the water and the vehicle moves at a velocity greater than that of sound. High peak pressures occur at the point of initial contact which may result in local damage to the structure. The flow line establishment phase starts after the initial contact and lasts until the flow about the structure becomes quasi-steady. The overall forces and accelerations on the body have been considered to be most important during this phase. The following sections of this study will be concerned with the flow line establishment phase of the water entry phenomenon. The quasi-steady phase involves the formation and collapse of a cavity, depending on vehicle geometry, as the vehicle becomes more completely submerged in the water. Several forces, including bouyancy, gravity, and drag become important during this phase, but are not considered over the shorter periods of the first two phases.

The most commonly used theory to determine water impact loads during the flow establishment phase is based on very early work (1929) by Theodore von Karman (Ref 3). The equations used assume conservation of momentum of the vehicle mass and a varying mass (virtual mass) of water which moves beneath the vehicle. However, in this early work and in the more recent publications on water impact loads the theoretical treatment has been limited to rigid bodies. Because the present analytical methods are limited to predicting rigid body force-time histories, it has been necessary for the NASA to determine design loads on the Apollo Command Module during water impact through experimentation using models and full scale test vehicles (Ref 4:1282-1284). The NASA experimental programs have included tests with rigid and elastically

scaled models. Results from the NASA programs have demonstrated that model test data and theoretical analysis compare favorably when the model is rigid. However, in one program the bottom of the model was made flexible. The resulting peak loads at the model center of gravity were nearly doubled (see Fig. 1). In Ref 4, Benson, of the Manned Spacecraft Center, concluded that analysis to accommodate structural flexibility and oblique landings is needed to investigate the large numbers of parameters that can occur.

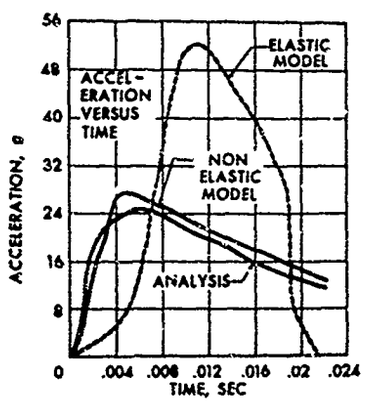

Figure 1

Comparison of Model Tests and

Theoretical Analysis (From Ref 4)

Purpose and Scope

The purpose of this study is to extend present water impact theory for the flow line establishment phase to include the effects of a flexible structure. The extension includes dynamic coupling between the water pressure (hydrodynamic forces) and the elastic and inertial forces of the structure. An objective of the present study is to see if a very elementary theoretical model, with two degrees of freedom, will provide an increase in accuracy in the prediction of dynamic responses and loads from water impact.

This study has been limited to vertical flight paths into water (no oblique landings) and simple spherically shaped elastic structures. Since the purpose is to increase accuracy in theoretical load prediction methods, parameters involving complex structural geometry have, in the initial study, been minimized. In order to assess the accuracy of the theoretical methods developed, the study has included tests with variations in loadings and flexibility of an elastic model.

Section II presents a review of present theory for a rigid body entering water and develops additional equations of motion for the flexible body. A modified theory is presented which considers the flexibility of a spherical shell. The experimental part of the study is presented in Sections III and IV. In Section V a comparison of theory and test results is presented. Sections VI and VII contain the conclusions of the study and some recommendations for future studies of this nature. Details of the theoretical and experimental parts of the study are presented in Appendices A through D.

II. Theoretical Development

Rigid Body Entering Water

The following theory applies to the Flow Line Establishment Phase. This phase has been considered to be the most critical with respect to overall forces and accelerations on the body. The equations presented are from the very early theoretical work of T. von Karman (Ref 3), more recent work by the NASA (Ref 5) and the summary of governing equations by Collopy (Ref 2).

The classical impact theory by von Karman applies to the vertical impact of a wedge (Fig. 2(a)) as it strikes a horizontal surface of water. Let: M = the mass of the body per unit length,

α = the angle of inclination of the under surface with the horizontal,

y = the vertical distance through which the body travels in time, t, and

$2r = 2y \cot \alpha$ = the corresponding breadth of the part of the body in the water.

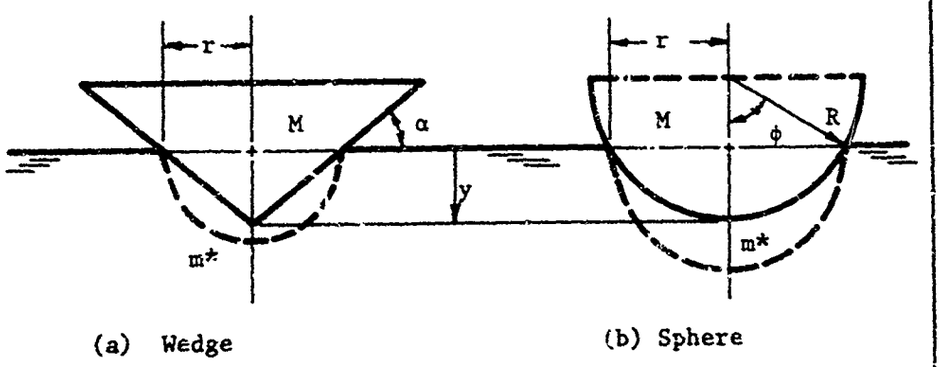

(a) Wedge (b) Sphere

Figure 2

Geometry for Bodies Entering Water

During the course of an impact, the momentum lost by the impacting body is considered as transferred to an imaginary or virtual mass (m^*) of water in contact with the body. The virtual mass of water has a downward velocity equal to that of the body. Hence, the entire initial momentum of the body is assumed to be distributed between the body and the virtual mass of water; the momentum is constant throughout the impact.

The following assumptions have been made.

1. Gravity force, bouyant force, friction drag, viscosity, and surface tension effects are neglected.

2. The body shell is rigid and the fluid is incompressible.

3. Momentum is conserved for the system of body and water.

The governing equation may be written as

$$MV_o = (M + m^*)\,\dot{y} \tag{2.1}$$

where V_o is the velocity of the body at the moment of first contact and $\dot{y}$ is the velocity at any time, t. Equation (2.1) may be rewritten as

$$\dot{y} = \frac{V_o}{1 + m^*/M} \tag{2.2}$$

Von Karman proposed that the virtual mass be taken equal to the mass of a semicylinder of water having a diameter equal to the instantaneous width of the body in the plane of the undisturbed water surface. The virtual mass per unit length of the wedge may be written as

$$m^* = \frac{1}{2}\, r^2 \rho \pi \tag{2.3}$$

where ρ represents the density of the water. If r^2 in equation (2.3) is expressed in terms of y and α and the results are substituted into

equation (2.2), the following equation is obtained:

$$\dot{y} = \frac{V_o}{1 + \frac{\rho \pi y^2 \cot^2 \alpha}{2M}} \tag{2.4}$$

NASA engineers (Ref 5) applied the above theory (Equation 2.2) to three-dimensional bodies with spherical lower surfaces to investigate the water-landing characteristics of reentry capsules. It was assumed that the virtual mass could be taken equal to three-quarters of the mass of a hemisphere of water having a diameter equal to the instantaneous width of the body in the plane of the undisturbed water surface. The arbitrary factor of three-quarters was an approximate correction indicated to be desirable by data from the impact of wedges (Ref 6). For the spherical body, the virtual mass was written as

$$m^* = \left(\frac{3}{4}\right) \frac{2\pi}{3} \rho r^3 \tag{2.5}$$

The body geometry for a sphere entering water is shown in Fig. 2(b). The instantaneous radius r can be expressed in terms of depth y and radius of the sphere R as

$$r = (2Ry - y^2)^{1/2}$$

or

$$r = R\left(\frac{2y}{R} - \frac{y^2}{R^2}\right)^{1/2} \tag{2.6}$$

and the virtual mass may be written as

$$m^* = \frac{\pi \rho R^3}{2}\left(\frac{2y}{R} - \frac{y^2}{R^2}\right)^{3/2} \tag{2.7}$$

When equation (2.7) is substituted into equation (2.2), the velocity of the spherical body becomes:

$$\dot{y} = \frac{V_o}{1 + \frac{\pi\rho R^3}{2M}\left(\frac{2y}{R} - \frac{y^2}{R^2}\right)^{3/2}} \tag{2.8}$$

Two important factors should be pointed out. The first is that equation (2.2) can be applied to any general shape if an expression can be obtained for the appropriate virtual mass and its rate of change as the depth of penetration changes. The second factor is that past investigators of water entry phenomena have used quite a variety of constants in the expressions for the virtual mass, even for the case of a sphere entering water. Reference 7 considers the sphere and other axisymmetrically shaped bodies. The virtual mass in each case is considered as $0.32\pi\ (4/3)\ \rho r^3$, where r is the instantaneous radius at the surface of the water. Collopy (Ref 2) and Mosteller (Ref 1) quote $4/3\ \rho r^3$ as a very common figure found in much of the literature. Lamb (Ref 8:123-125) indicates that the virtual mass for a sphere is $2/3\ \pi\rho r^3$. In this study, the virtual mass will be considered as that indicated by equation (2.7) except where a change is indicated in following sections.

Equation (2.2) can be differentiated to obtain an expression for the vertical acceleration. Differentiation of equation (2.2) results in

$$\ddot{y} = \frac{-V_o}{\left(1 + \frac{m^*}{M}\right)^2}\left(\frac{1}{M}\right)\frac{dm^*}{dt} \tag{2.9}$$

since

$$\frac{dm^*}{dt} = \frac{dm^*}{dy}\frac{dy}{dt} = \dot{y}\frac{dm^*}{dy}$$

Equation (2.9) can be written

$$\ddot{y} = \frac{-V_o}{\left(1 + \frac{m^*}{M}\right)^2}\left(\frac{1}{M}\right)\dot{y}\frac{dm^*}{dy} \tag{2.10}$$

The force acting on the body can be written as

$$F = M\ddot{y} = \frac{-V_o}{\left(1 + \frac{m^*}{M}\right)^2} \dot{y} \frac{dm^*}{dy} \tag{2.11}$$

If equation (2.2) is substituted into equation (2.11), the force may be expressed as

$$F = \frac{-V_o^2}{\left(1 + \frac{m^*}{M}\right)^3} \frac{dm^*}{dy} \tag{2.12}$$

For any particular geometry, the vertical component of average pressure is equal to the force divided by the instantaneous area of the body in the plane of the undisturbed water surface.

The force on a spherical body may be obtained by substituting equation (2.7), for the virtual mass, into equation (2.12). The rate of change of virtual mass may be written as

$$\frac{dm^*}{dy} = \left(\frac{3}{2}\right) \frac{\pi\rho R^3}{2} \left(\frac{2y}{R} - \frac{y^2}{R^2}\right)^{1/2} \left(\frac{2}{R} - \frac{2y}{R^2}\right) \tag{2.13}$$

and

$$F = \frac{-\frac{3}{2} \pi\rho R^2 V_o^2 \left(1 - \frac{y}{R}\right) \left(\frac{2y}{R} - \frac{y^2}{R^2}\right)^{1/2}}{\left[1 + \frac{\pi\rho R^3}{2M} \left(\frac{2y}{R} - \frac{y^2}{R^2}\right)^{3/2}\right]^3} \tag{2.14}$$

It can be seen from equation (2.14) that the maximum force along the y-axis varies as the square of the vertical contact velocity for a given radius and mass. Variations in the force corresponding to changes in the radius and mass are not quite so apparent from inspection of the equation.

When the mass of the body is large compared to the virtual mass of water (i.e., when a heavy, slender missile enters the water

vertically), then the term $\pi\rho R^3/2M$ is small and the denominator of equation (2.14) is approximately equal to 1.0. This approximation has been used frequently in the past, but it is not applicable for a blunt body such as a space capsule.

If equation (2.14) is differentiated with respect to y/R and the derivative is set equal to zero, the resulting equation indicates the depth of penetration at which the maximum force occurs. Let the term $\pi\rho R^3/2M = C$. Then, from $\frac{dF}{dy/R} = 0$, the following equation may be obtained:

$$\left[1 + C\left(\frac{2y}{R} - \frac{y^2}{R^2}\right)^{3/2}\right]\left[\left(1 + \frac{y}{R}\right)^2 - \left(\frac{2y}{R} - \frac{y^2}{R^2}\right)\right]$$

$$= 9C\left(1 - \frac{y}{R}\right)^2\left(\frac{2y}{R} - \frac{y^2}{R^2}\right)^{3/2} \qquad (2.15)$$

Equation (2.15) may be transformed into a transcendental equation in terms of the angle ϕ, where ϕ is shown in Figure 3.

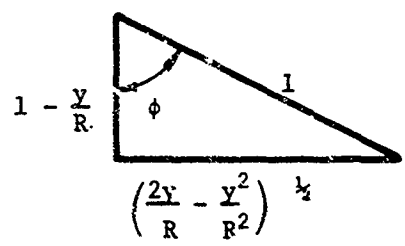

Figure 3

Angle ϕ

(From Ref. 2)

The maximum force occurs when

$$\frac{1}{C\sin^3\phi} + 1 = \frac{9}{1 - \tan^2\phi}$$

The foregoing theoretical results are illustrated in Figures 4 through 6. A comparison between theoretical and experimental acceleration time histories for a reentry capsule having a segment of a sphere as its lower section is shown in Figure 4. These results were obtained by the Langley Research Center (Ref 5:26). The full scale capsule characteristics were: Weight = 2150 lbs, Radius of spherical bottom = 10.5 ft, Base diameter = 7.0 ft, and the Entry velocity, V_o = 30 fps. Reference 5 states that the model (1/12 scale) was constructed of fiber glass and plastic and the construction was as rigid as possible to eliminate secondary vibrations. The base of the full scale capsule was formed from 1.00 inch magnesium alloy. In the theoretical computations, the expression for the virtual mass was as indicated in equation (2.7).

Figures 5 and 6 apply to a small rigid sphere entering water Figure 5 shows the theoretical time-histories of displacement and velocity; figure 6 shows the corresponding acceleration and average vertical pressure. The body characteristics and initial conditions were: Weight = 30 lbs, Radius = 2 ft, and Velocity = 20 fps. These characteristics were selected for more detailed analyses in the following section (Flexible Bodies Entering Water) and also for the experimental part of this study (see Section III).

Theoretical computations for the curves of Figures 5 and 6 were made using the AFIT IBM 1620 Digital Computer. The equations used, table of results, and plotted curves for different body characteristics and initial velocities are presented in Appendix A.

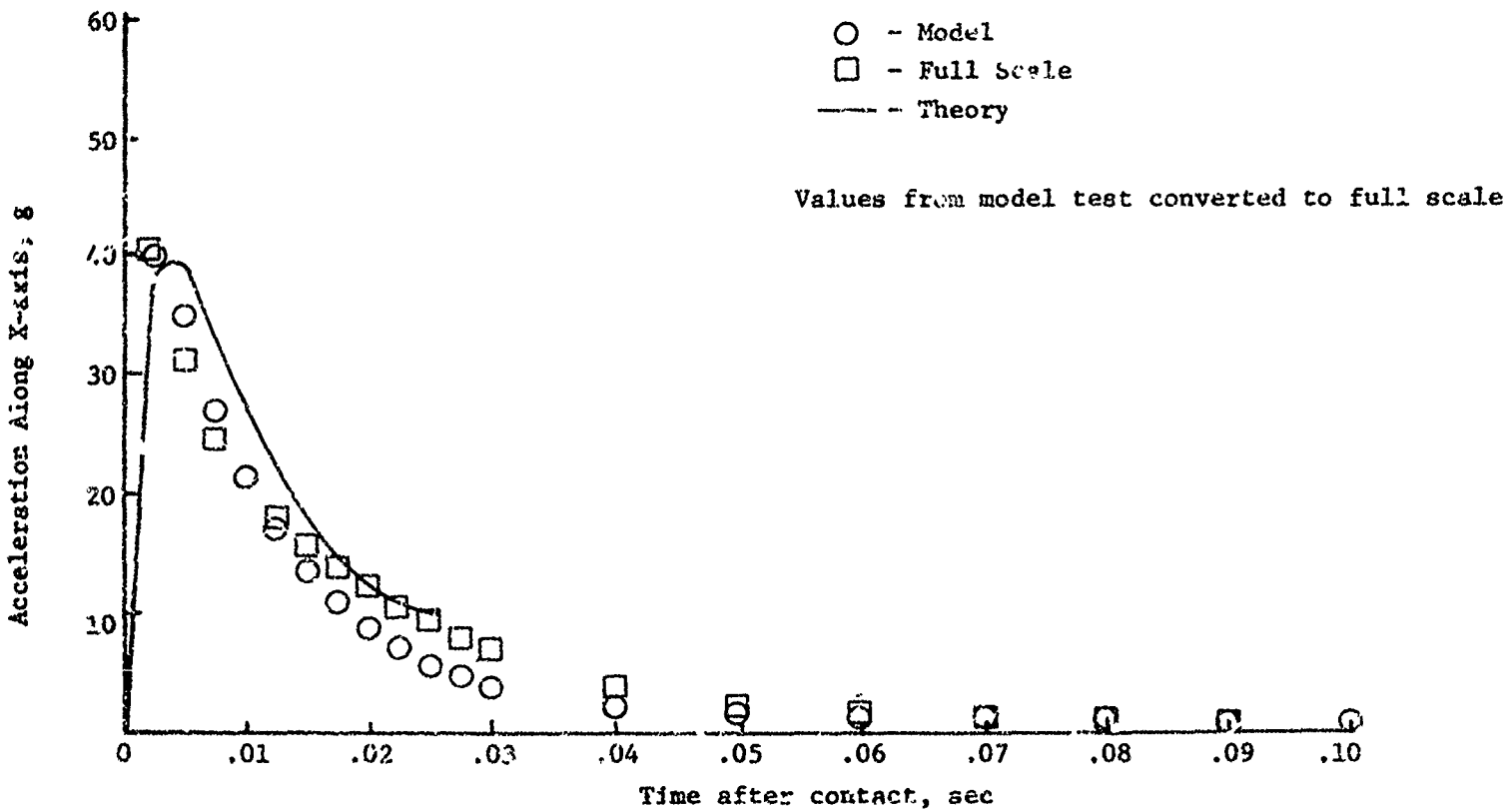

Figure 4

Comparison of Acceleration-Time Histories Obtained from Model Test, Full-Scale Test, and Theoretical Investigation. (Flight Path, 90°; Contact Attitude, 0°.)

(From: Ref 5:26)

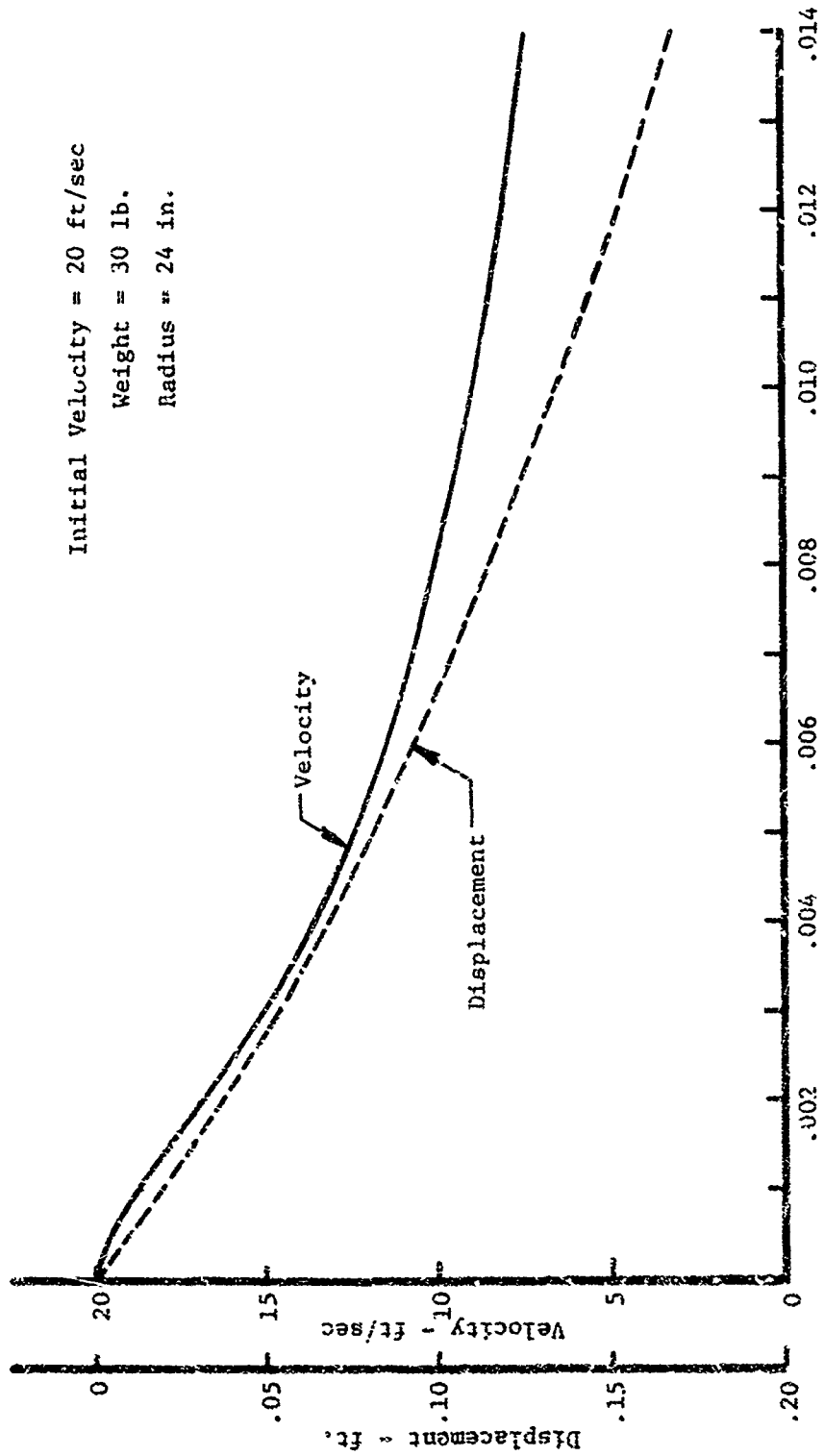

Figure 5

Time Histories of Velocity and Displacement for a Rigid Body Entering Water

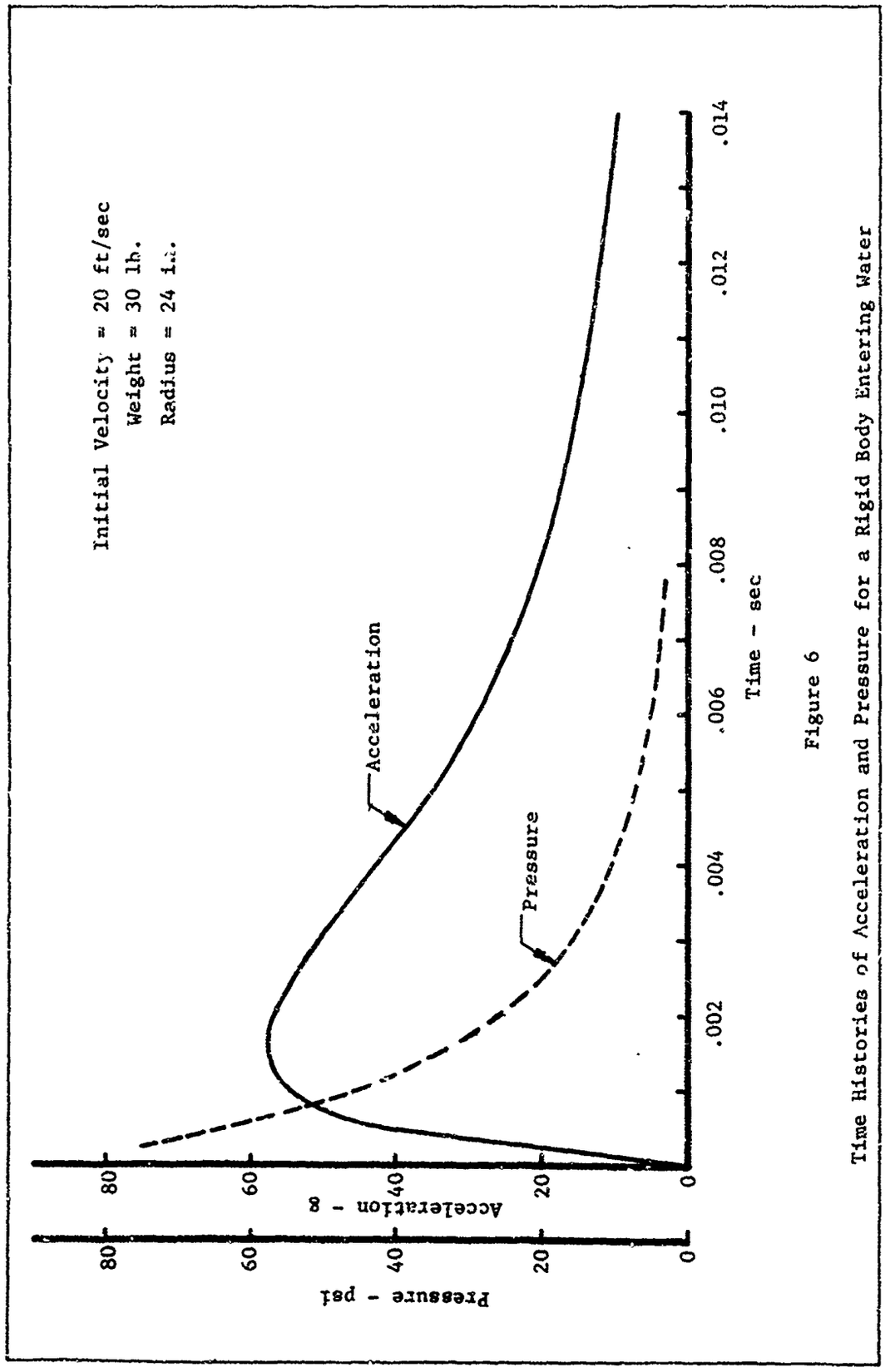

Figure 6

Time Histories of Acceleration and Pressure for a Rigid Body Entering Water

Flexible Body Entering Water

A basic assumption in the foregoing theory for a rigid body entering water was that the body and virtual mass of water move with the same velocity. The forces involved were the inertia force due to the rigid body and the reaction force due to the acceleration of the virtual mass of water. This reaction force caused a sudden reduction in the velocity of the body.

During the impact period when a flexible body (structure) enters water, the change in velocity of the wetted surface of the body which is in contact with the water may be quite different than the change in velocity at the center of mass of the flexible body. Hence, the effective velocity of the virtual mass of water, which moves with the wetted surface of the flexible body, would also be different than the velocity at the center of mass of the flexible body. The forces involved now consist of the flexible body inertial and elastic forces combined with the reaction force due to the acceleration of the virtual mass of water. Furthermore, the rate of change in the size of the virtual mass is a function of the deformed shape of the flexible body. For small deflections, this may not be an important factor. However, for large deflections the rate of change in virtual mass could be considerably different than that calculated from the original shape of the body (see Figure 27, Appendix A, which shows the effect on acceleration of changing the shell radius).

The problem of a flexible body impacting on water may be treated approximately in the following manner. Consider a body with an elastic spherically shaped shell as the under surface. The dynamic

characteristics of the upper structure may become very significant for a particular type geometry or vehicle. However, in this study, the upper structure is treated only as a lumped mass at the center of gravity. When the elastic shell strikes a horizontal surface of water, the pressure causes the shell to deflect upward through a distance, δ_o, measured from the lower center of the undeformed geometry as shown in Figure 7.

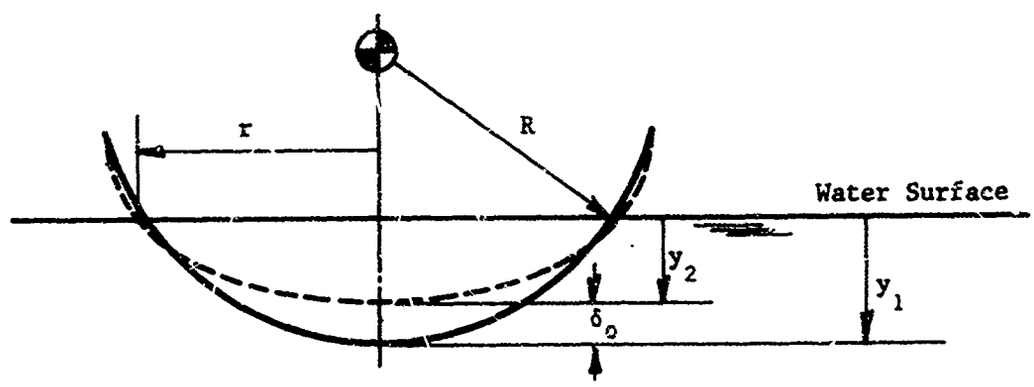

Figure 7

Flexible Shell Coordinates During Water Impact

The principle of conservation of momentum may be applied, as in the case of a rigid body, except that it is now necessary to consider two coordinates to account for the velocity of the center of mass and the velocity of the lower elastic shell. The momentum theorem may be written as follows:

$$MV_o = M_R \dot{y}_1 + M_e (\dot{y}_1 - \dot{\delta}_o) + m^* (\dot{y}_1 - \chi\dot{\delta}_o) \qquad (2.17)$$

where:

M = total mass of the body

M_R = mass of the upper structure and undeformed portions of the shell (rigid mass)

M_s = mass of the deformed parts of the wetted shell considered as concentrated at the shell lower center

$\dot{y}_1$ = velocity of the center of mass

$\dot{\delta}_o$ = deflection velocity at the lower center of the shell

χ = a fraction between 0. and 1.0 which reduces the center deflection velocity to the mean or effective velocity of the wetted surface

Since $M_R + M_s = M$, equation (2.17) may be rewritten as

$$MV_o = (M + m^*)\ \dot{y}_1 - (M_s + \chi m^*)\ \dot{\delta}_o \qquad (2.18)$$

When the mass distribution of the elastic shell is known, the value of M_s can be approximated by assuming a deflection shape and calculating an equivalent value of mass, concentrated at the lower center, which would provide approximately the same momentum as the distributed mass in the deformed part of the shell. However, the distribution of the virtual mass of water is unknown. The effective velocity of the virtual mass is between the values of $\dot{y}_1$ and $\dot{y}_2$ as shown in Fig. 7. Since the entire virtual mass is not affected evenly by the center deflection velocity $\dot{\delta}_o = \dot{y}_1 - \dot{y}_2$, an effective deflection velocity $-\chi\dot{\delta}_o$ has been included in the above equations. This is discussed in greater detail in Appendix B, where it is shown that the value of χ may be approximately 2/3 or greater based on deflection shapes for thin spherical shells.

In the following analyses, equation (2.18) has been simplified by assuming that M_s is small compared with the virtual mass m^*. At time $t = 0$, both M_s and $m^* = 0$. However, immediately after the shell contacts the water, the value of m^* increases much faster than the value

of M_s for a thin shallow spherical shell. The deformed part of the shell does not extend appreciably beyond the radius of m* (see Appendix B). Therefore, the ratio M_s/m^* immediately after contact with the water is on the order of

$$\frac{M_s}{m^*} \approx \frac{2\pi R Y_1 h \rho \text{(structure)}}{\frac{\pi}{2} r^3 \rho \quad \text{(water)}}$$

where r is defined by equation (2.6), R = the shell radius, and h = the shell thickness. For the following conditions:

(Aluminum shell) $h = 0.04$ inches

$V_o = 20$ ft/sec

$W = 30$ lb

$R = 24$ inches

the value of M_s/m^* is approximately 0.13 at time t = 0.00025 seconds following initial contact with the water. Also, in the following analyses, an arbitrary value of 1.0 has been used for χ. With these changes, the conservation of momentum equation may be written as

$$MV_o = (M + m^*)\,\dot{y}_1 - m^*\,\dot{\delta}_o \tag{2.19}$$

Rewritten, equation (2.19) becomes

$$\dot{v}_1 = \frac{V_o + \frac{m^*}{M}\dot{\delta}_o}{1 + \frac{m^*}{M}} \tag{2.20}$$

As a first approximation, it is assumed that the virtual mass and its rate of change can be computed based on the undeformed shell geometry. This approximation should be valid for small deflections. However, it is believed that the virtual mass would actually be increased slightly due to shell deformations.

In order to solve equation (2.20) it is necessary to know the deflection of the shell, as a function of time or depth of penetration, due to the reaction force of the virtual mass of water. Figure 8, obtained from Reference 4, shows pressure distributions that were measured on a model with a spherical bottom during the Apollo water impact development program. Although the pressure is slightly higher at the outer edge of the wetted under surface than at the center, not too great an error is made in assuming that the reaction force produces a uniform pressure loading. This assumption of uniform pressure has been used in the following section to determine the approximate spring stiffness for a spherical shell.

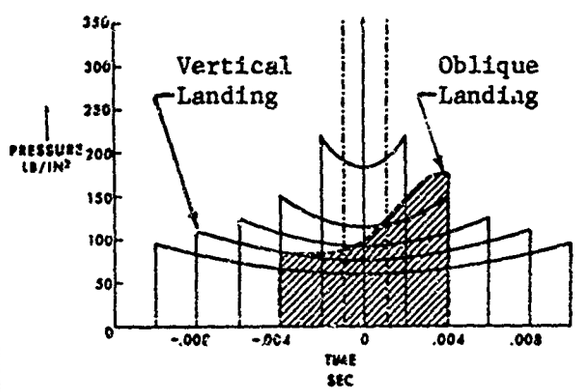

Figure 8

Typical Pressure Pattern Growth

(From Ref 4)

Spring Stiffness for Shallow Spherical Shell

Reference 9:558-561 treats the symmetrical bending of shallow spherical shells (see Fig. 9). When a point load P is applied at the apex, the deflection of the shell at the point of application of the load is given by (notation as used in Ref 9)

$$w_o = \frac{\sqrt{3\ (1-\nu^2)}}{4}\ \frac{Pa}{Eh^2} \tag{2.21}$$

where

ν = Poisson's ratio

E = Young's modulus

a = shell radius (Same as R in previous equations)

h = shell thickness

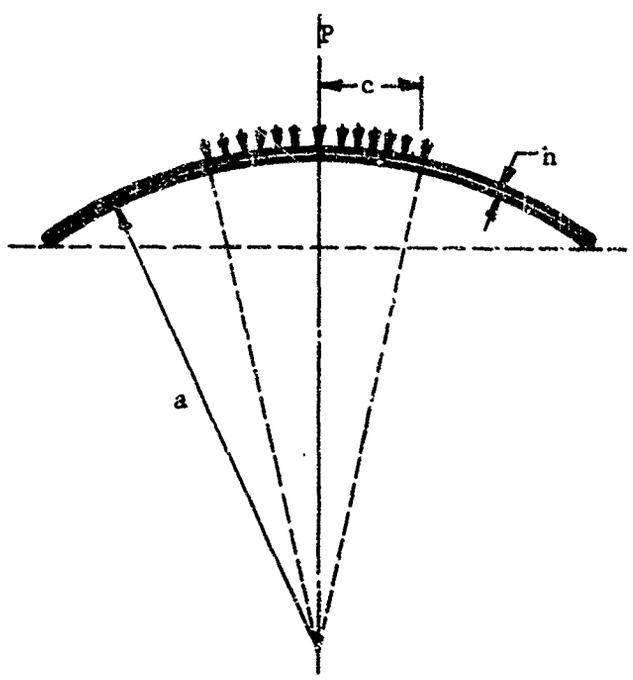

Figure 9

Shell Geometry

When the central load P is uniformly distributed over a circular area of a small radius c, the following results apply at the center of the loaded area:

$$w_o = \frac{\sqrt{12(1-\nu^2)}}{\pi} \frac{Pa}{Eh^2} \left[\frac{1}{\mu^2} - \frac{\pi}{2\mu} \psi_4'(\mu) \right] \tag{2.22}$$

where

$$\mu = \frac{c}{\ell} = \frac{c \sqrt[4]{12(1-\nu^2)}}{\sqrt{ah}}$$

$$\ell = \frac{\sqrt{ah}}{\sqrt[4]{12(1-\nu^2)}} = \text{characteristic length for spherical shell}$$

$$\psi_4'(\mu) = \frac{d\psi_4(\mu)}{d\mu}$$

The function ψ_4' is developed in Ref 9:488-492. Values of ψ_4' are tabulated in Ref 9 for values of the argument, in the case of μ, up to 6.0. Ref 9 states that for values of the argument above 6.0, the following asymptotic expression is sufficiently accurate:

$$\psi_4'(\mu) = \sqrt{\frac{2}{\pi\mu}} \; e^{-\mu/\sqrt{2}} \cos\left(\frac{\mu}{\sqrt{2}} - \frac{\pi}{8}\right) \tag{2.23}$$

In the expression for $\mu = c/\ell$, ℓ is a characteristic length for the shell. The authors state, "when ℓ as defined above is small compared with the radius of the edge, this is equivalent to the case of a plate on a very rigid foundation. The deflections and the bending moments at the center of such a shell are affected very little by the respective conditions on the outer edge, which only govern the state of the edge zone of the shell."

The shell loading conditions for equation (2.22) are similar to those for a shell impacting on the surface of water. Shortly after the shell strikes the surface, the pressure is distributed over a small portion of the shell. However, it should be pointed out that static shell theory is being applied to a dynamic problem. Also, the equation is complicated and it cannot be applied directly to obtain a closed form solution when values of ψ_4' are significant.

A brief investigation was made to determine values of μ and ψ_4' for different values of c, a, and h in equation (2.22). For fixed values of shell radius and thickness, μ is directly proportional to c (c is the same as r in earlier equations). If Poisson's ratio is taken as 0.3, then

$$\mu = 1.818 \frac{c}{\sqrt{ah}} \tag{2.24}$$

As the shell penetrates into the water, c and μ increase in value. It can be seen from tabulated values of the function ψ_4' (Ref 9:493-494) that ψ_4' decreases from plus infinity ($\mu = 0$) to zero ($\mu = 2.67$). Then ψ_4' reaches a maximum negative value of -0.0213 ($\mu = 3.60$) followed by an increase toward zero for larger values of μ. The function ψ_4' does not exceed ±0.0213 for values of μ above approximately 2.40. Therefore, the function ψ_4' in equation (2.22) is most significant for the very small values of c. However, there is a fairly wide range of values of μ for which ψ_4' is very small and could be omitted in equation (2.22) without incroducing serious error in the results. Table 1 shows how values of μ increase with increasing values of c for various values of the product ah.

Table I

Calculated Values of the Parameter μ

Projected Radius of the Applied Uniform Load c	Product of Shell Radius and Thickness axh	Parameter μ
.5000	.5000	1.2854
.5000	1.0000	.9089
.5000	1.5000	.7421
.5000	2.0000	.6427
.5000	2.5000	.5749
1.0000	.5000	2.5708
1.0000	1.0000	1.8178
1.0000	1.5000	1.4843
1.0000	2.0000	1.2854
1.0000	2.5000	1.1497
2.0000	.5000	5.1416
2.0000	1.0000	3.6357
2.0000	1.5000	2.9685
2.0000	2.0000	2.5708
2.0000	2.5000	2.2994
4.0000	.5000	10.2833
4.0000	1.0000	7.2714
4.0000	1.5000	5.9370
4.0000	2.0000	5.1416
4.0000	2.5000	4.5988
8.0000	.5000	20.5665
8.0000	1.0000	14.5427
8.0000	1.5000	11.8741
8.0000	2.0000	10.2833
8.0000	2.5000	9.1976

If it is assumed that ψ_4' in equation (2.22) is equal to zero, the resulting equation is much simpler and the deflection at the center of the loaded area can be written as

$$w_o = \frac{P\,a^2}{\pi c^2\,Eh} \tag{2.25}$$

Since $P/\pi c^2$ is the vertical component of the pressure acting on the shell, equation (2.25) can be written

$$\delta_o = \frac{pR^2}{Eh} \tag{2.26}$$

where $\delta_o = w_o$ = shell deflection at the center of the applied load

$R = a$ = shell radius

p = average applied pressure

Equation (2.26) is an approximate expression for the shell deflection which applies only for a uniform pressure which is distributed over a sufficiently large area such that ψ_4' can be neglected. The applicability of equation (2.26) to obtain the shell spring stiffness for use in the water impact problem was checked in two ways. First, values of μ and ψ_4' were calculated for a structure with a spherical under surface entering water. The following parameters were used:

Shell radius, $R = 24$ in

Weight, $w = 30$ lb

Shell thickness, $h = .03$ in, .04 in, .05 in

Contact velocity, $V_o = 20$ fps

Modulus of elasticity, $E = 10.5 \times 10^6$ psi

The depth of penetration, y_1, radius of the applied pressure, c, acceleration and pressure were calculated using the equations previously developed for a rigid body. Calculations were performed on the

AFIT IBM 1620 digital computer for time increments of 0.00025 seconds. The value of the ratio of the second term to the first term in the brackets of equation (2.22) was determined as a measure of the error if the term involving ψ_4' is neglected. In other words:

$$E = \%\ \text{ERROR} = 100 \left[\frac{\frac{\pi}{2\mu}\ \psi_4'(\mu)}{1/\mu^2} \right]$$

When μ was less than 6.0, values of ψ_4' were obtained from Table 84, Ref 9. However, when μ was greater than 6.0, ψ_4' was calculated using equation (2.23). Results of this analysis are shown in Table II. The function ψ_4' is quite small, even after the first time increment of .00025 seconds, and it is observed that the error in neglecting ψ_4' should not exceed approximately 12 percent. The negative sign in Table II for E indicates that the calculated values of δ_o are low using the approximate equation (2.26) Deflections for the shell with thickness, h, equal to .04 inches are shown in Table II for the first ten Δt time increments.

The second check on equation (2.26) was to compare the deflections obtained from this equation with those obtained using matrix techniques. Reference 10 presents a technique for analyzing axisymmetrical shell structures subjected to general loading conditions, using the Matrix Displacement Method. Structures are idealized by truncated conical shell elements and circular flat plate elements, joined together at nodal circles. A computer program to solve the matrix equations is available in Fortran IV language for the IBM 7094 computer at Wright-Patterson AFB. For the present problem, a spherical shell segment with a 24 inch radius and a 24 inch base chord was analyzed.

Table II

Data for the Evaluation of Shell Deflections

Time t (sec)	Depth of Penetration y_1 (in)	Radius of Loading c (in)	Parameter μ	Parameter ψ_4'	ERROR E %	Shell Deflection δ_o (in)
0	0	0	0		-	0
0.00025	0.0600	1.696	3.15	-0.0171	- 8.5	0.104
.00050	.1194	2.392	4.44	- .0163	-11.4	.092
.00075	.1780	2.917	5.41	- .0074	- 6.4	.075
.00100	.2352	3.352	6.22	- .0030	- 2.0	.063
.00125	.2912	3.728	6.92	- .0000 (1)	- 0.0 (2)	.053
.00150	.3458	4.060	7.53	.0000	0.0	.046
.00175	.3991	4.359	8.09	.0000	0.0	.040
.00200	.4510	4.631	8.59	.0000	0.0	.034
.00225	.5015	4.881	9.06	.0000	0.0	.030
.00250	.5507	5.112	9.48	.0000	0.0	.027

(1) - Where only zeros are shown, the value of ψ_4' was less than .0005.

(2) - Where only zeros are shown, the value of E was less than 0.5%.

The shell segment was considered as fixed at the outer edge. The shell segment was divided into 12 elements, for purposes of analysis, and the applied pressures were calculated using the equations presented in this study for various depths of penetration. A comparison of results is presented in Table III; the angles used are shown in Fig. 10.

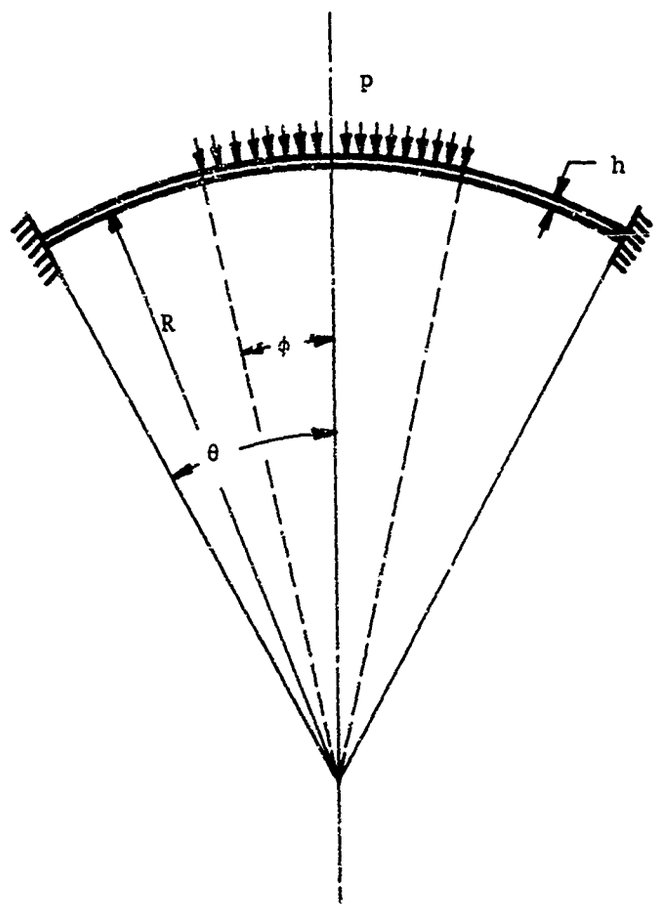

Figure 10

Shell Edge Support and Loading For Calculation of Deflections by Matrix Methods

Table III

Deflections and Buckling Pressures for a Spherical Shell

Penetration Depth y_1 (in)	Loading Angle ϕ (deg)	Applied Pressure p (psi)	Shell Thickness h (in)	Buckling Pressure (psi)		Linear Deflection (in)	
				Matrix Method	Theory (1)	Matrix Method	Theory (2)
.060	4.05	75.50	.03	20.18	19.85	.1441	.138
.235	8.03	45.78	.03	18.17		.0866	.084
.346	9.72	33.32	.03	18.38		.0603	.061
.501	11.72	22.06	.03	18.39		.0387	.040
.823	15.05	10.41	.03	18.35		.0169	.019
.060	4.05	75.50	.04	40.31	35.29	.1012	.104
.235	8.03	45.78	.04	33.19		.0658	.063
.346	9.72	33.32	.04	33.71		.0451	.046
.501	11.72	26.06	.04	33.91		.0286	.030
.823	15.05	10.41	.04	33.83		.0125	.014
.060	4.05	75.50	.05	70.02	55.14	.0758	.083
.235	8.03	45.78	.05	52.88		.0533	.050
.346	9.72	33.32	.05	53.57		.0363	.037
.501	11.72	26.06	.05	54.16		.0226	.024
.823	15.05	10.41	.05	54.11		.0098	.011

Radius = 24 inches

θ = 30 degrees

(1) Values Calculated from Eq. (2.29)
(2) Values Calculated from Eq. (2.26)

Table III shows that deflections calculated using equation (2.26) compare favorably with those from the matrix displacement method. As a matter of interest, critical buckling pressures were also calculated using classical theory for the condition of uniform pressure over a sphere and the results are shown in Table III together with the calculated buckling pressures using the matrix displacement method of Ref 10. These results were considered in the model design and testing part of the present study. From small deflection theory, as summarized in Ref 11, the average stress, σ, of a spherical shell at the critical buckling pressure is defined by

$$\sigma = \frac{pR}{2h} \tag{2.27}$$

the buckling stress may also be expressed by

$$\sigma = \frac{E\ h/R}{\sqrt{3\ (1-\nu^2)}} \tag{2.28}$$

For Poisson's ratio of 0.3, the expression for critical buckling pressure of a spherical shell becomes

$$p_{cr} = 1.21\ E\ \frac{h^2}{R^2} \tag{2.29}$$

Equation (2.29) was used for the theoretical buckling values shown in Table III. If the above expression for critical buckling pressure, equation (2.29), is substituted into equation (2.26), the following expression is obtained for the limiting deflection which would not exceed the allowable buckling deflection

$$\delta_o = 1.21h \tag{2.30}$$

Equation (2.26) can be used to define a spring stiffness for a spherical shell. The equation can be rewritten in terms of the force,

P, (see Eq. 2.25) as

$$\delta_o = \frac{P R^2}{\pi c^2 E h} \tag{2.31}$$

If the spring stiffness, K, is defined as

$$K = \frac{P}{\delta_o} \tag{2.32}$$

then, by substituting equation (2.31) into equation (2.32), the expression for K becomes

$$K = \frac{\pi Eh c^2}{R^2} \tag{2.33}$$

The spring stiffness is a function of the projected loading radius c. For small deflections, c can be expressed in terms of y_1 and R (see Eq. 2.6) and K can be expressed as

$$K = \pi Eh \left(\frac{2y_1}{R} - \frac{y_1^2}{R^2}\right) \tag{2.34}$$

It should be noted that equation (2.34) is not valid when y_1 is near zero. In this case, a value for K can be obtained from equation (2.21) which applies for a concentrated load (c = 0). From the above definition of K and Equation (2.21) which defines the deflection when c = 0, the expression for K is

$$K_{c=o} = \frac{4 Eh^2}{\sqrt{3(1-\nu^2)}R} \tag{2.35}$$

Figure 11 shows the theoretical spring stiffness as developed from the preceding equations for an aluminum shell entering water with the following shell characteristics: R = 24 in, h = 0.04, E = 10.5 x 10^6 psi. The transition from equation (2.21) to equation (2.22) is shown for small vaules of y_1; the effects of ψ_4' were considered in the

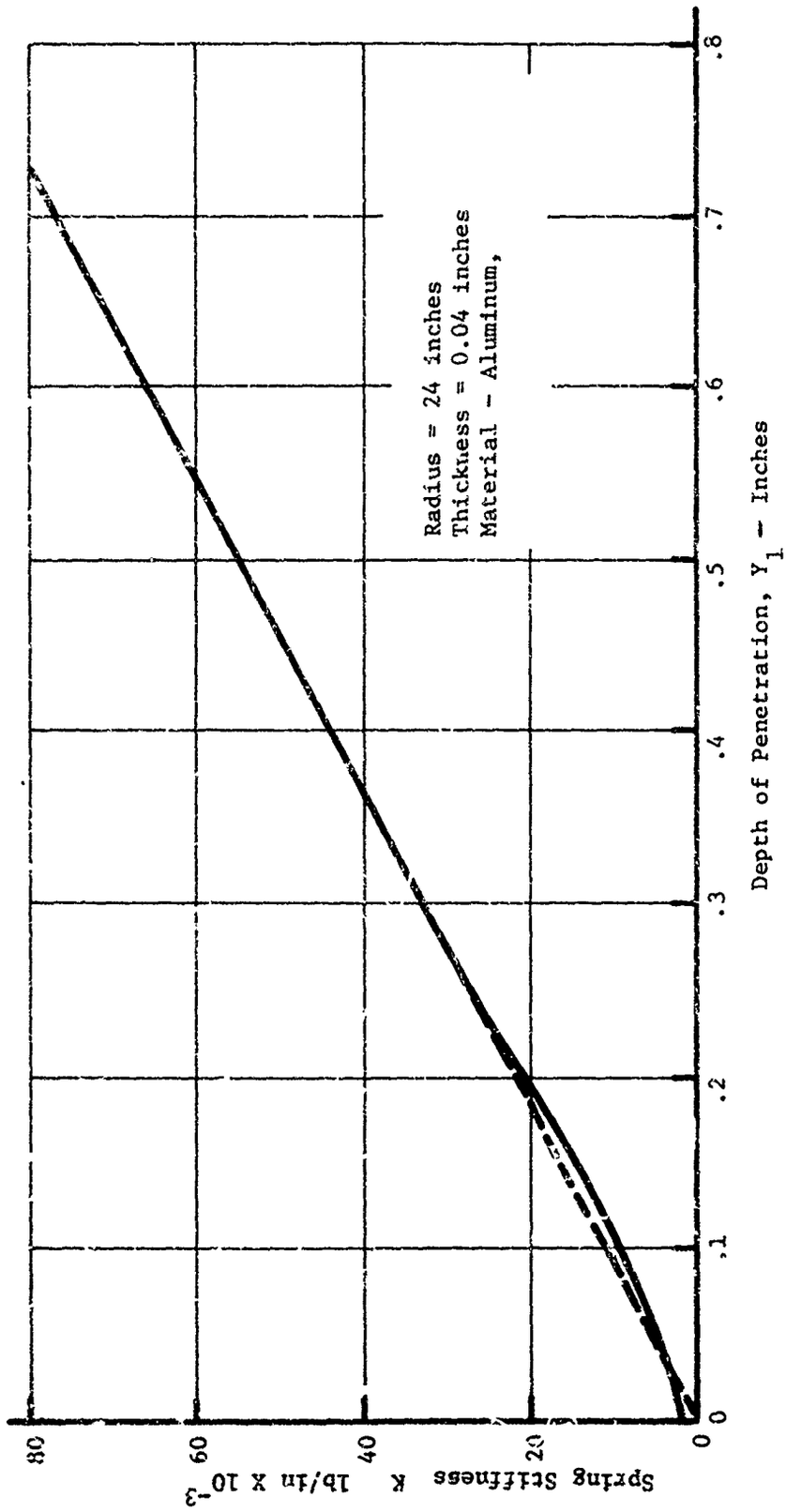

Figure 11

Spring Stiffness for a Spherical Shell Entering Water

calculation of δ_o. It can be seen that a linear extension of K calculated from Eq (2.26) deviates only slightly from the more exact curve, even for the very small values of y_1. The spring rate would become softer for large values of y_1 due to the second term $(-y^2/R^2)$ in equation (2.34). However, this effect would normally be beyond the depths of interest in the water impact problem.

Solution of Differential Equations by the Runge-Kutta Method

The equations of motion previously developed for the flexible shell structure entering water are repeated below as

$$MV_o = M\dot{y}_1 + m^* (\dot{y}_1 - \dot{\delta}_o) \tag{2.36}$$

$$\delta_o = P/K \tag{2.37}$$

Equations (2.36) and (2.37) may also be written in terms of the coordinate y_2 (see Fig. 7) as

$$MV_o = M\dot{y}_1 + m^* \dot{y}_2 \tag{2.38}$$

and

$$y_1 - y_2 = P/K \tag{2.39}$$

where, as before, it is assumed that the shell deflection velocity is equal to $\dot{\delta}_o$ all along the wetted under surface. If equation (2.38) is differentiated with respect to time, the following expression is obtained for the body inertial and hydrodynamic reaction forces:

$$0 = M\ddot{y}_1 + m^* \ddot{y}_2 + \dot{m}^* \dot{y}_2 \tag{2.40}$$

or

$$-M\ddot{y}_1 = m^* \ddot{y}_2 + \dot{m}^* \dot{y}_2 \tag{2.41}$$

Equation (2.41) represents the appropriate expression for the force P in the above equations. The left hand side of equation (2.41) may

be substituted for P in equation (2.37). Also, the right hand side of equation (2.41) may be substituted for P in equation (2.39). The resulting sets of differential equations may then be written as

$$\dot{y}_1 = \frac{V_o + \frac{m^*}{M}\dot{\delta}_o}{1 + \frac{m^*}{M}} \tag{2.42}$$

$$\ddot{y}_1 = -\frac{K}{M}\delta_o \tag{2.43}$$

and

$$\dot{y}_2 = \frac{M}{m^*}(V_o - \dot{y}_1) \tag{2.44}$$

$$\ddot{y}_2 = \frac{1}{m^*}\left[K(y_1 - y_2) - \dot{m}^*\dot{y}_2\right] \tag{2.45}$$

The above sets of equations may be rearranged, and through substitutions, a third order nonlinear differential equation may be obtained. However, in this study the solutions were obtained using the Runge-Kutta method for solving simultaneous differential equations. A program is available at AFIT (AFIT AID PROGRAM 236) for obtaining solutions on the digital computer. The standard aid program was modified slightly for the present study in order to obtain desired quantities such as acceleration, force, and pressure during each computer run. The Runge-Kutta program is discussed briefly in Appendix B. Equations (2.42) and (2.43) were used for the

analyses in this study with the appropriate expressions for m* and K as functions of y_1. However, equations (2.44) and (2.45) were also programmed and run on the computer for the 0.04 thick shell to verify that the same shell deflection time-history would be obtained from either set of equations. The results agreed well; variations in results were generally less than one percent at each Δt time interval. The small differences obtained are due to the integration scheme used in the Runge-Kutta method.

Figures 12 through 14 show theoretical results for a spherical structure with the following characteristics impacting on water: Radius = 24 in, weight = 30 lb, shell thickness = 0.04 in, and contact velocity = 20 fps. Appendix B presents the equations used and additional results from shells of different thickness.

The curves in Figures 12 and 13 show a comparison between the rigid body and flexible body velocities and accelerations. Figure 14 compares the dynamic deflection-time history with the corresponding shell deflections obtained from the rigid body pressure-time history. Since the equations for the flexible body do not contain any damping, the oscillations induced by the initial impact conditions do not decay. To check the effects of adding damping, a viscous damping term was added to equation (2.43). The damping force was made proportional to both $\dot{\delta}_o$ and the projected wetted area. The resulting equation may be expressed as

$$\ddot{y}_1 = -\frac{K}{M}\,\delta_o - \frac{c}{M}\,\dot{\delta}_o \qquad (2.46)$$

where c is the damping coefficient. c was considered to be a function of y_1 in a manner similar to K. An average damping ratio $\zeta = c/c_{cr}$ of approximately .0375 critical damping for the first cycle of oscillation

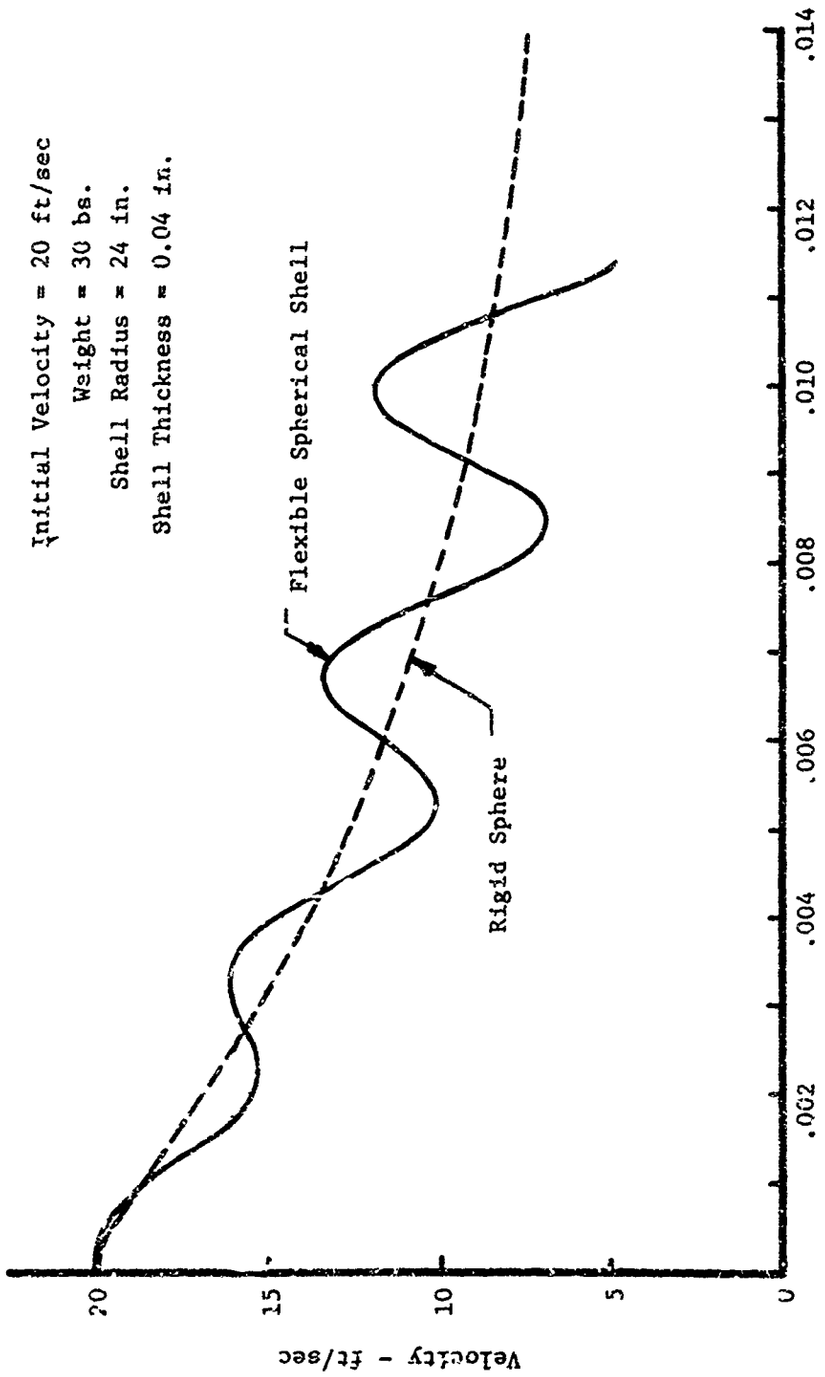

Figure 12

Comparison of Velocity - Time Histories for Rigid and Flexible Structures

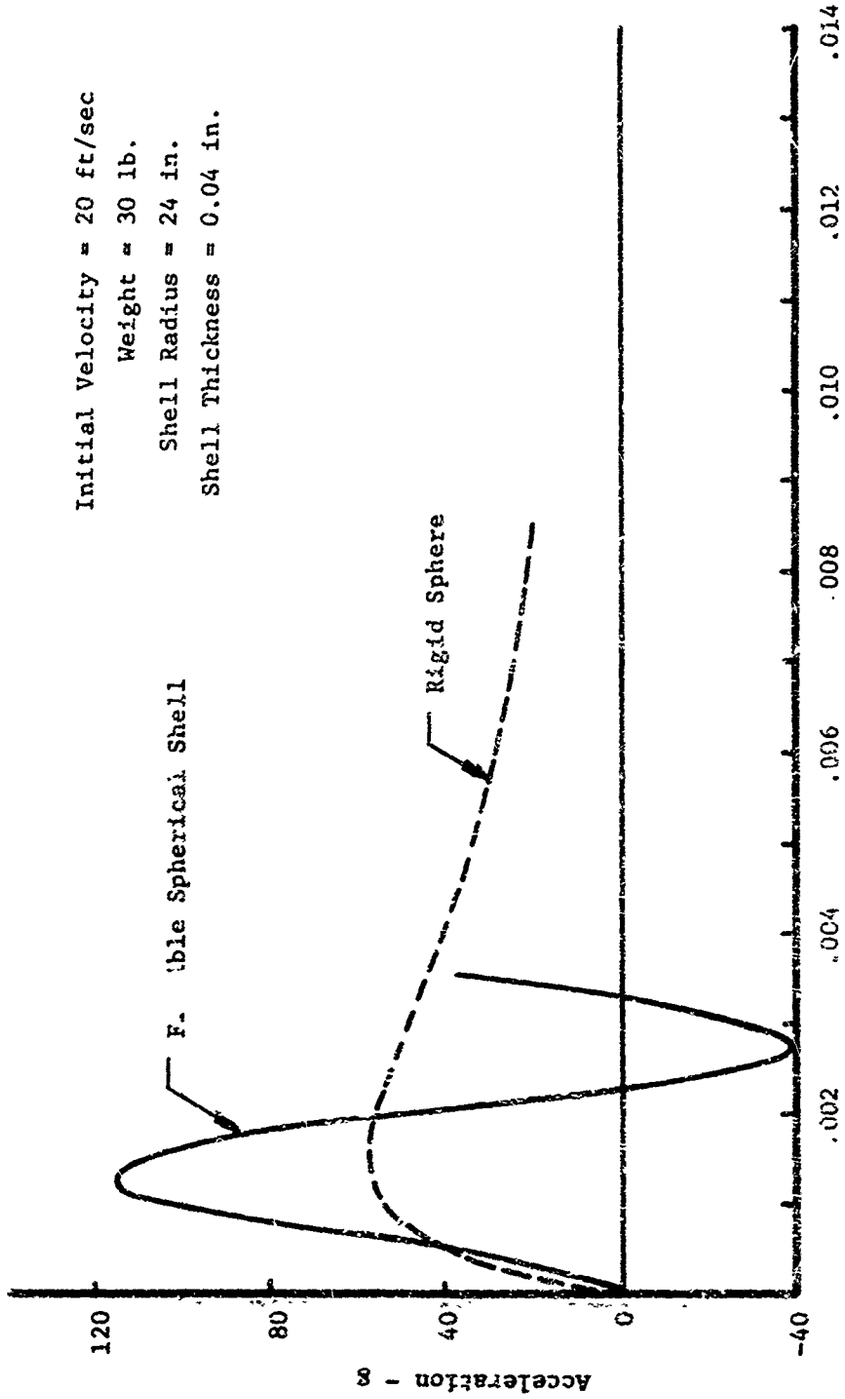

Figure 13

Comparison of Acceleration - Time Histories for Rigid and Flexible Structure

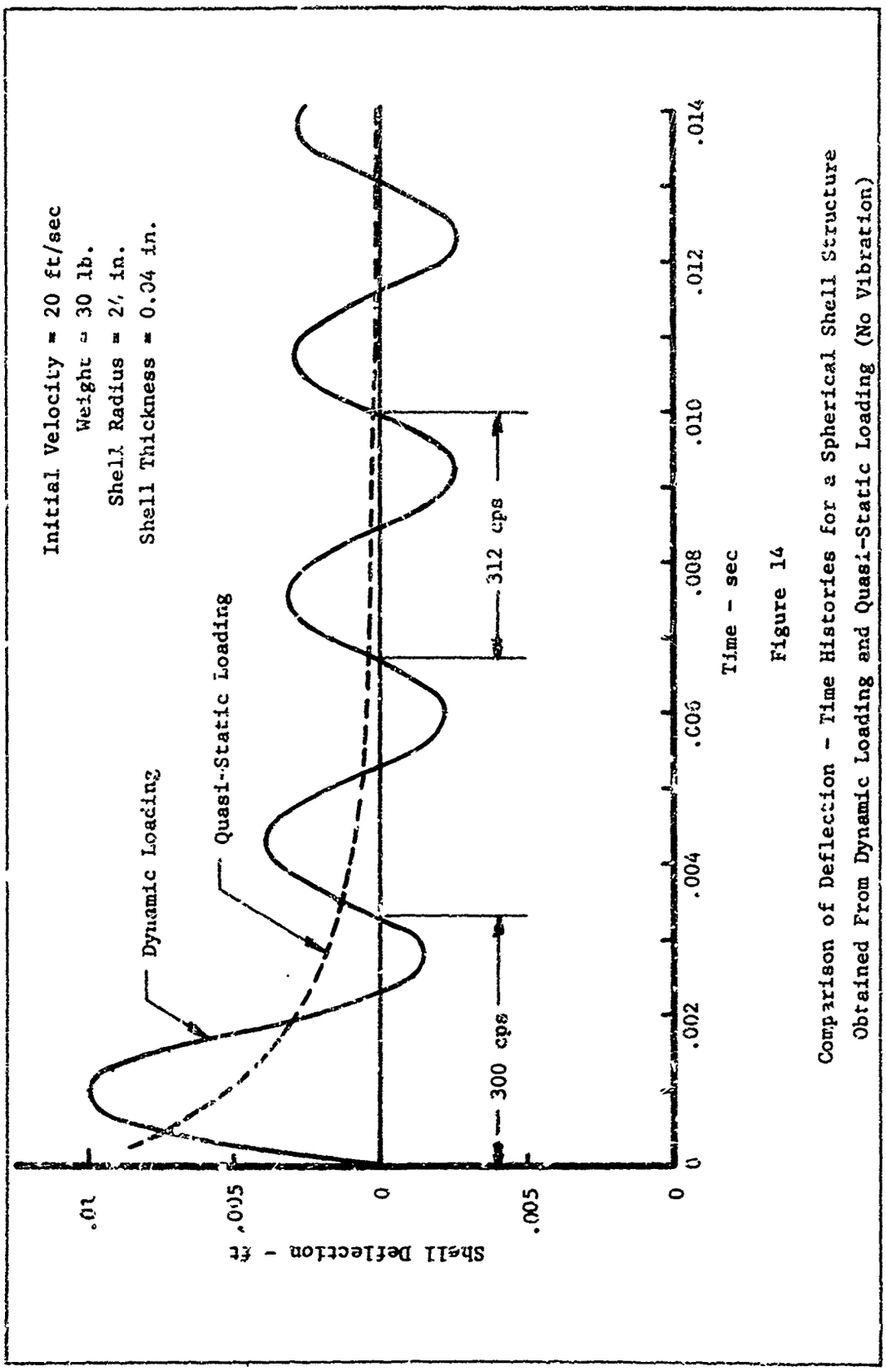

Figure 14

Comparison of Deflection - Time Histories for a Spherical Shell Structure Obtained From Dynamic Loading and Quasi-Static Loading (No Vibration)

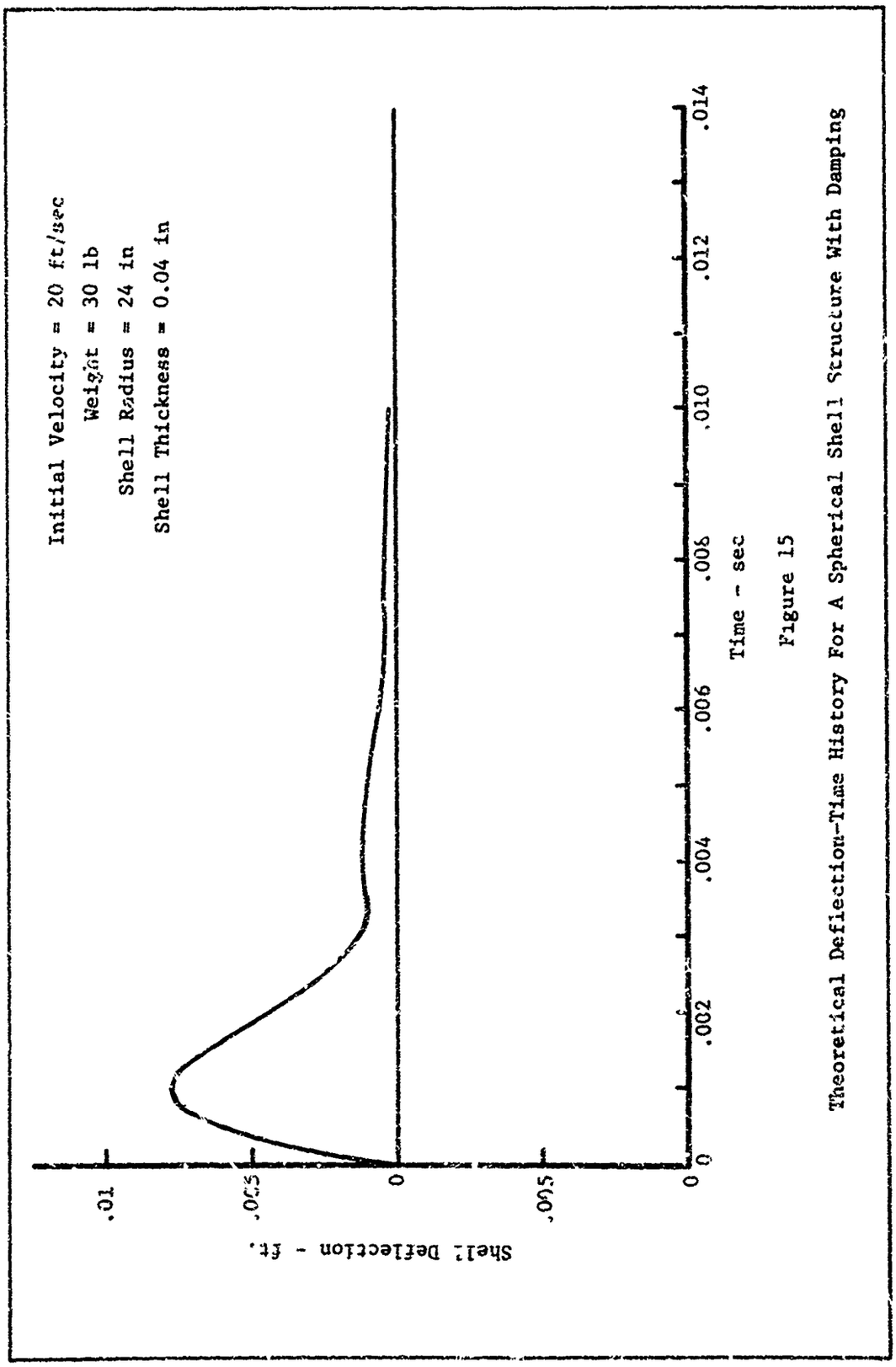

Figure 15

Theoretical Deflection-Time History For A Spherical Shell Structure With Damping

shown in Figure 14 produced the changes in the deflection time-history that are shown in Figure 15. As mentioned above, the value of c increased with time and depth of penetration. The damping ratio used was likely above that which would be realized in actual situations. However, no further investigations of damping were made in the present study.

It is interesting to note that the frequency of the oscillations in Figure 14 increases with time. This change in frequency is rather complex corresponding to the changes in the shell spring rate and to the changes in the virtual mass of water. The behavior of the system, consisting of the structural mass and virtual mass, appears to be similar to the two degree of freedom system shown in Figure 16. The center of mass moves from the structural mass toward the virtual mass.

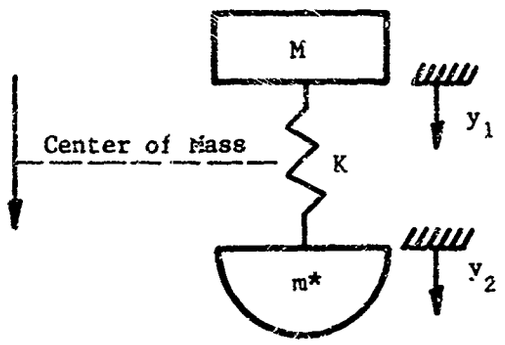

Figure 16

Model of Two Degree of Freedom System

When the virtual mass is equal to the structural mass, the center of mass is mid-way between the two and the effective spring rate is equal to 2K. For the curve in Figure 14 the two masses were equal when the depth of penetration, y_1, was equal to 0.114 ft. The natural frequency of the system at this point was calculated to be 314 cps. The average frequency of oscillation at this point in Figure 14 was found to be 312 cps. Over an interval of 0.022 seconds, the frequency changed from 300 cps to 251 cps. These frequencies were obtained from the plotted deflection-time history.

As previously indicated, equations (2.42) and (2.43) were used in this study to obtain the time histories of response shown in Figures 12 through 14. The velocity and acceleration curves correspond to the motion at the center of mass. The deflection-time history presented corresponds to the relative deflection between the c.g. and the center of the shell lower surface. Although the successive oscillations of the relative deflection remain fairly constant in amplitude after the initial impact (without damping), the successive oscillations in velocity and acceleration at the c.g. increase in amplitude over several cycles of oscillation. It is considered that this effect is due to the downward shift in the center of mass of the system in combination with the requirement for conservation of momentum of the total system (structural mass and virtual mass). However, more complete studies of the system using equations (2.44) and (2.45) are needed for a complete understanding of the overall responses and accelerations of the system.

The Runge-Kutta format that was used to enable evaluating the relative deflection from equations (2.44) and (2.45) is presented in Appendix B. Time did not permit a more complete study of the lower surface (and virtual mass) responses and accelerations. Appendix B also contains additional discussion of the c.g. acceleration and a figure which shows the acceleration-time history for a thick shell over a longer time period.

III. Experimental Apparatus and Procedure

Model Design and Instrumentation

As mentioned in the introduction, experiments were conducted to enable an evaluation of the theory developed in Section II for water-landing impact accelerations on flexible bodies. A sketch of the dynamic model that was constructed and tested in shown in Figure 17. Figure 18 is a photograph of the actual test model. The model was made of aluminum and it consisted of three basic parts: (1) a thin upper cylinder, 24 inches in diameter and 24 inches high, with a closed top, (2) a 1/2 inch thick plate, 24 inches in diameter, with cut-outs to facilitate installing response measuring instruments, and (3) a thin lower spherical shell segment with the shell radius and chord equal to 24 inches. The upper cylinder functioned only as a means for suspending the model and for attaching guides along two sides to prevent tumbling during the model decent into the water. a stiffener and eye bolt were fastened to the top for raising the model. The primary weight of the model was the aluminum plate. It was intended that this section be fairly rigid. The upper cylinder and the lower shell were fastened to vertical and beveled edges of the plate. Four spherical shells were formed by the Sheet Metal Branch, Directorate of Maintenance, WPAFB by pressing sheet aluminum into a mold. The shells were formed from 2024 aluminum; they were hardened to approximately T4 after forming. The nominal shell thicknesses were .032, .040, .050, and .080 inches. The model weight was 29.75 lbs with the .080 inch thick shell installed. In order to keep the total weight nearly constant during the tests, additional weight

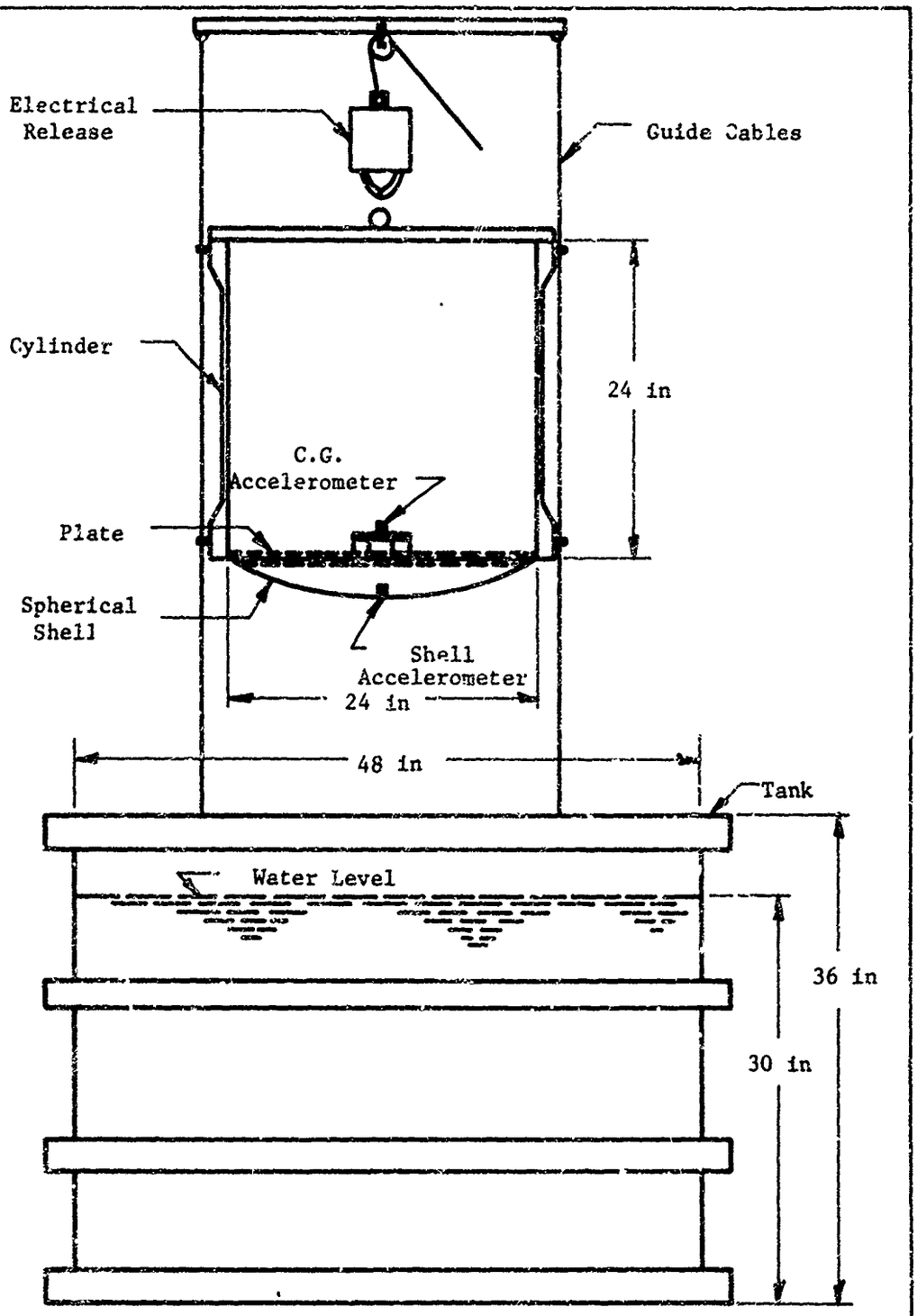

Figure 17

Sketch of the Water Impact Test Set-Up

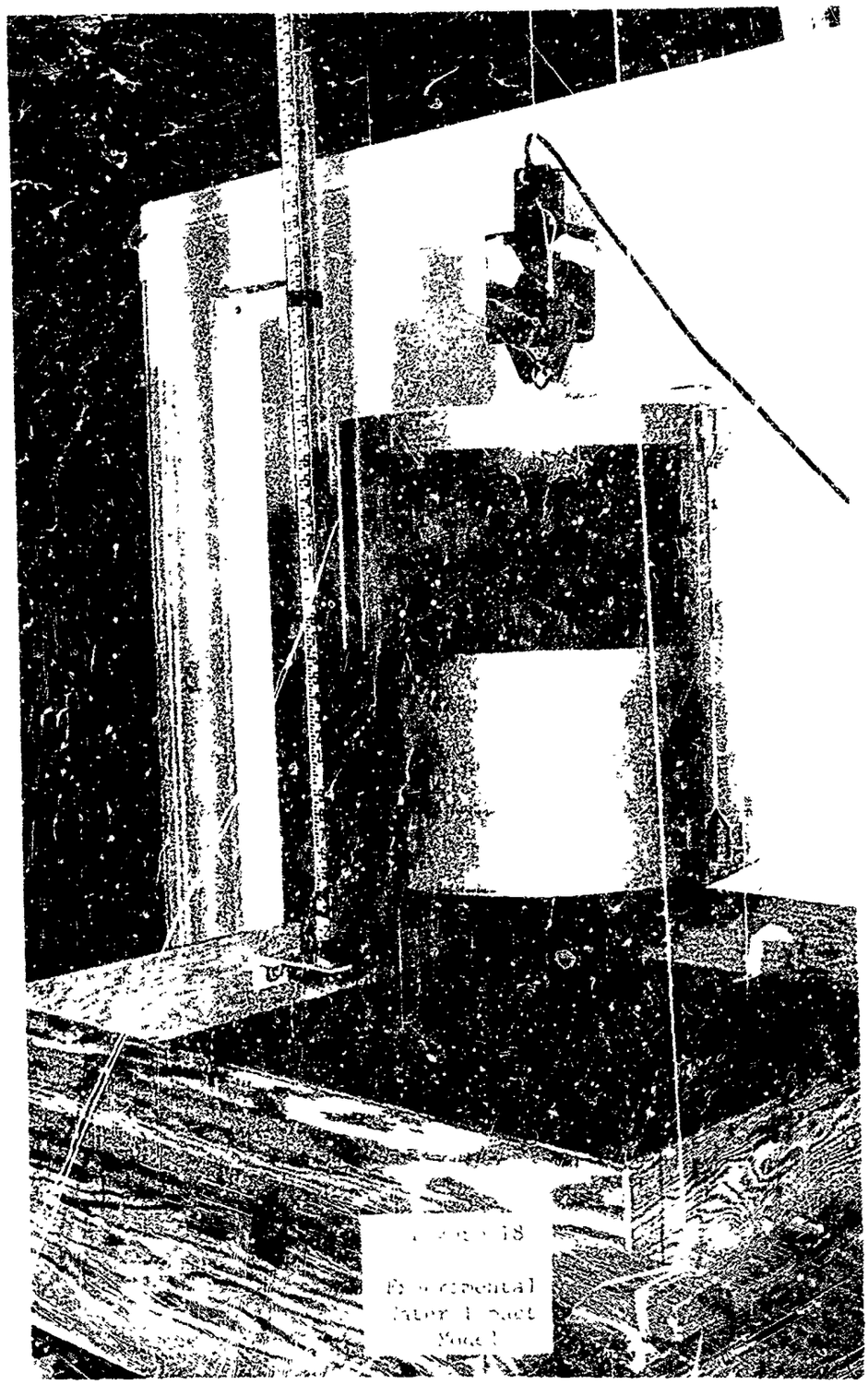

was added to the plate when the 0.40 in thick shell was installed to keep the overall weight at 29.75 lbs. The added weight was not changed during testing with the .032 in and .050 in thick shells. The model weight was 29.4 lb and 30.2 lbs with the .032 in and .050 in thick shells respectively.

Two accelerometers were located in the model to measure impact accelerations. One accelerometer was located approximately one inch above the center of the 1/2 inch plate on a stiff bracket to measure c.g. accelerations. It was originally intended that shell deflections would be measured using strain gages mounted on a thin curved column that was fastened to the shell and protruded through an opening in the plate to a bracket above the plate. Hence, the c.g. accelerometer was mounted above this column bracket. However, the strain gage column was not calibrated in time for the tests and a second accelerometer was therefore mounted at the center of the shell to measure the shell accelerations.

Water Impact Test Set-Up

The test set-up used is shown in Fig. 17. Vertical cables 1/16 in. in diameter were used to keep the model approximately vertical during free fall. The model was raised by a means of a rope and a pully mounted to the ceiling in the test laboratory. An electrically operated release hook, obtained from a conventional impacting testing machine, was used for releasing the model. The water tank used was constructed of wood and fiberglass; the tank dimensions are shown in Figure 17.

Description of Acceleration Measuring Equipment

A block diagram of the test instrumentation is shown in Figure 19. Figure 20 shows a photograph of the instrumentation as it was set up during the test program. Piezoelectric type accelerometers were used; the signals from the accelerometers were transmitted through cables to amplifying and recording equipment. Also, the accelerometer signals were transmitted to an oscilloscope where the signals were subtracted. The difference in the signals was transmitted through a frequency analyzer, where a double integration was performed, and thence to the recorder. The purpose of this step was to provide a means for recording the shell deflection relative to the c.g. of the model. The system was calibrated first with the accelerometer signals in phase; the strength of the signals was balanced to provide a zero difference at the input to the oscilloscope. Then the accelerometers were mounted on the calibrator 180 degrees out of phase to enable obtaining a calibration for the relative deflection. The resonant frequency of the accelerometers was 28 KC, or higher, and the frequency response was flat (within 5 percent) to 5 KC. However, the linearity of the overall system was much more limited. Filters were used to significantly reduce the signals at frequencies of vibration above 1000 cps. The overall system was linear (within ±2 percent) to about 800 cps. A detailed list of the instrumentation characteristics is presented in Appendix D.

Test Procedure

Tests were conducted at vertical contact velocities of about 10 feet per second and 20 feet per second. The contact velocities

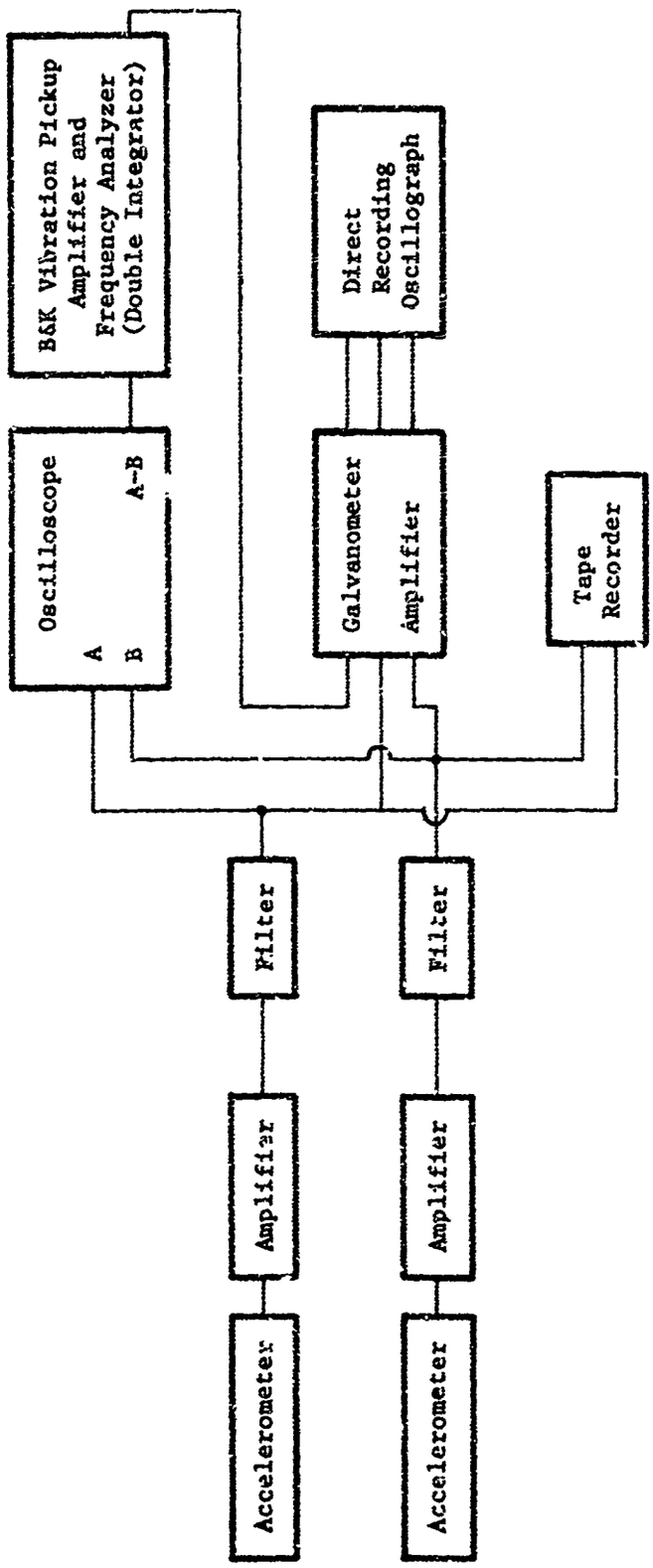

Figure 19

Block Diagram of Test Instrumentation

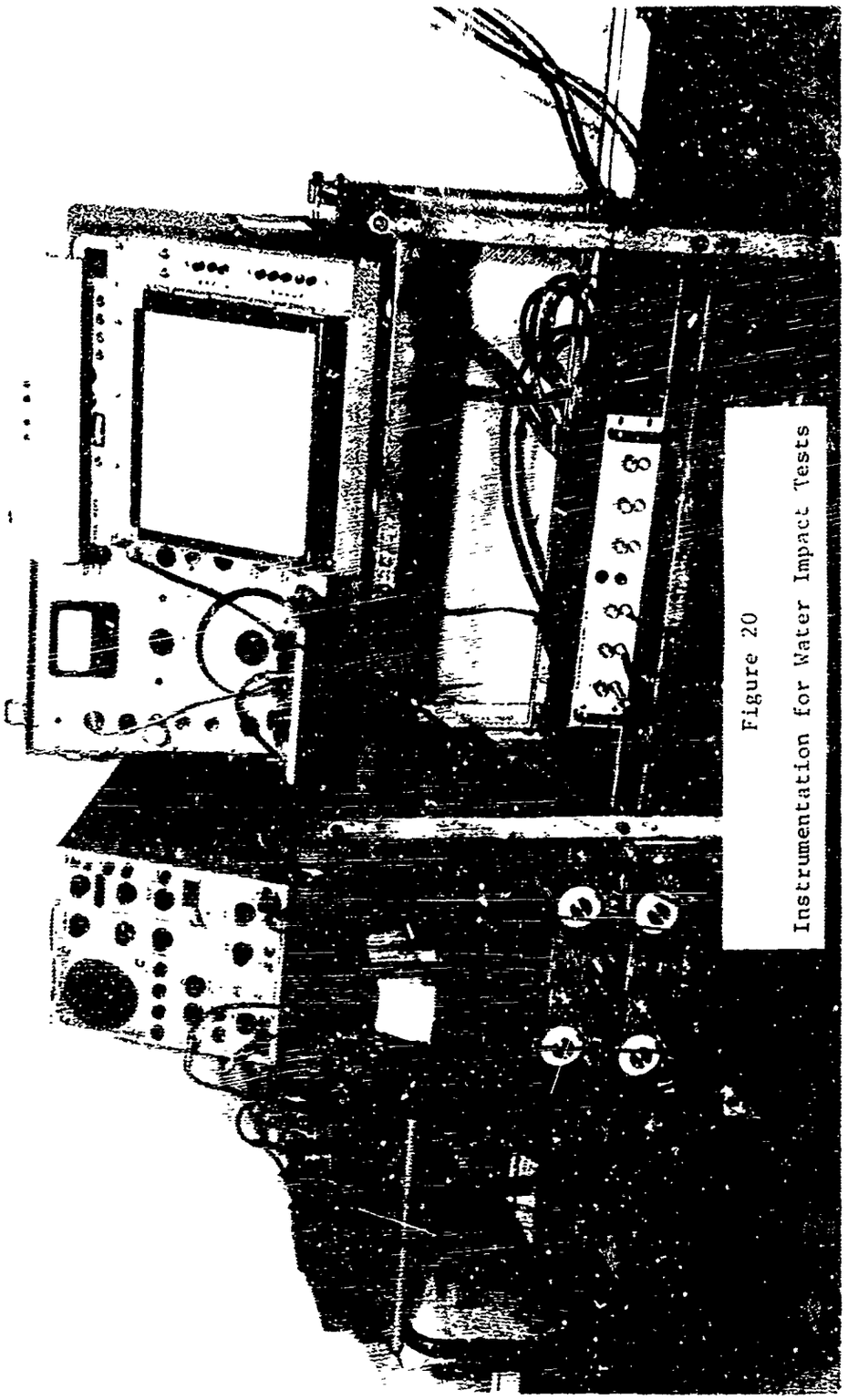

Figure 20

Instrumentation for Water Impact Tests

were obtained during the tests by using a high speed motion-picture camera. Figure 21 shows an enlargement of two frames from the high speed camera coverage of drop number 2. These two frames show the model before and after contact with the water. The model was raised and released from heights necessary to obtain the desired contact velocities based on calculated free-fall distances. Six drop tests were made; the test conditions for each drop are shown in Table IV.

During the test program, several changes were required in the instrumentation. Accelerometers were changed to reduce the output signals by a factor of approximately 4. Filters were installed and gain settings on the accelerometer amplifiers were reduced to the lowest settings possible. These changes required several intermediate equipment recalibrations. A final calibration was also performed to verify that all changes had been properly recorded.

Drops numbers 1, 2, and 3 were made primarily to check the instrumentation. The filters that were used in the instrumentation were installed between drops 2 and 3. Therefore, the previous description of the equipment was applicable for drops 3 through 6. Records obtained from the first 3 drops were not analyzed.

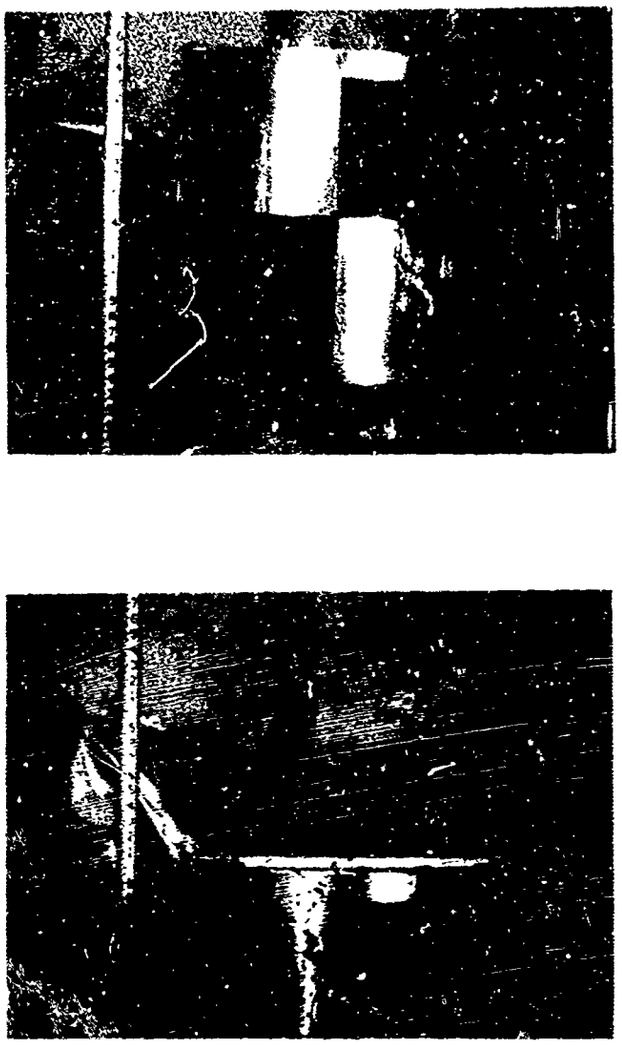

Figure 21

Experimental Model Before and After
Contact with the Water During Drop Test

Table IV

Water Impact Model Test Conditions

Drop No.	Contact Velocity Camera (ft/sec)	Contact Velocity Free Fall (Est.) (ft/sec)	Shell Thickness (in)	Model Weight (lb)
1	-	20	0.040	29.75
2	20.8	20	0.040	29.75
3	9.0	-	0.032	29.4
4	9.8	10	0.032	29.4
5	9.8	10	0.050	30.2
6	9.8	10	0.080	29.75

IV. Experimental Results and Discussion

Data Reduction Procedure

Past investigators of water impact loads have presented their experimental results in terms of the rigid body acceleration-time histories. Very little information is available on experiments with flexible structures. Reference 12 describes an experimental program wherein complex scale models (1/4.5 scale) were designed and tested to determine the structural responses of the Apollo Command Module to water impact. In the Apollo modeling program, a large number of high frequency vibrations were excited during impact and the experimental acceleration records obtained could not be reduced until the acceleration measuring system was modified to limit the system to a flat response from 0 - 600 cps. The data obtained were smoothed using a least-squares, 10th order polynomial and the resulting curves were presented in terms of the rigid body acceleration-time histories. The accelerations exhibited some oscillations, with positive and negative values, after the smoothing. The maximum sensitivity of the acceleration measuring system used in the experiments of Reference 12, expressed in terms of trace deflection on the oscillograph record for unit acceleration input, was about 0.03 inches/g.

In the present study, the experimental model was much less complicated than that of Reference 12 and it was hoped that any high structural responses would be at frequencies considerably above the frequency range of interest. However, this was not the case; the structural responses are discussed in the following section. Also it was considered that visual data reduction would be required in order to

obtain the transient, oscillatory components of response for comparison with the results obtained from the theoretical model.

Data from drop tests 1 and 2 could not be analyzed because of high frequency vibrations. Electrical filters were then placed in the acceleration measuring system to obtain a system which was flat to about 800 cps (see Section III). This change produced a more acceptable record for the c.g. acceleration during drop test number 3, but the record for the lower shell acceleration was overloaded indicating that the signal from this accelerometer was much too high. For subsequent testing (drops 4, 5, and 6), the overall sensitivity of the acceleration measuring system was reduced to 0.0125 inches/g. However, records for the lower accelerometer continued to be overloaded at approximately 210g for the first 3 to 5 cycles of response.

The overloaded condition for the lower (shell) accelerometer produced unacceptable results for integration to obtain the relative deflection of the lower shell. The final data reduction from drops 4, 5, and 6 consisted of the following:

(1) Response frequencies were obtained from both accelerometer traces. The accuracy with which oscillatory frequencies could be determined was satisfactory. The oscillograph was operated at a paper speed of 80 inches per second during testing and timing lines were one milli-second apart.

(2) Acceleration levels were obtained from the c.g. acceleration records. However, in order to obtain data which could be compared with the theoretical results it was necessary to perform a visual harmonic analysis of the records to remove structural responses corresponding to the additional degrees of freedom (natural frequencies of vibration) in

the test model. There are inaccuracies involved in making an harmonic analysis of a transient type response. However, the accuracy is considered to be within ± 20 percent. Figure 22 shows a tracing of the complex waveform from drop test number 5 and indicates the steps that were taken to determine the frequencies and amplitudes of the acceleration components. Figure 23 shows the reproduced complex wave which was obtained by adding three components with an assumed original phase relationship. This step was taken to check the adequacy of the data reduction procedure. The overall peak amplitude of the synthesized wave was ± 10 percent less than the original wave. Tracings of the original records for drop tests 4, 5, and 6 are contained in Appendix C.

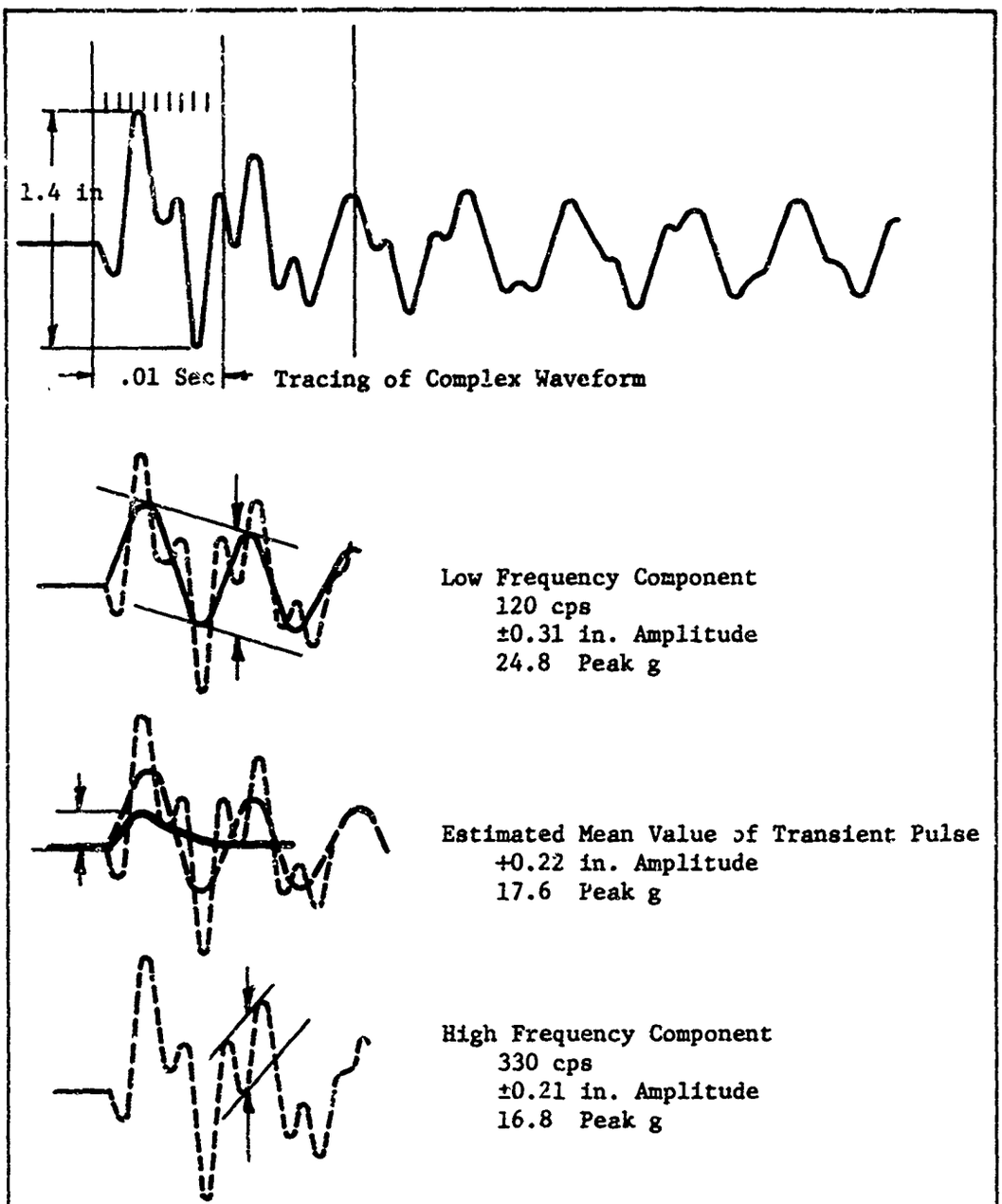

Note: Drop No. 5 c.g. Accelerometer
0.05 inch thick shell
V_o = 9.8 ft/sec

Figure 22

Data Reduction Procedure

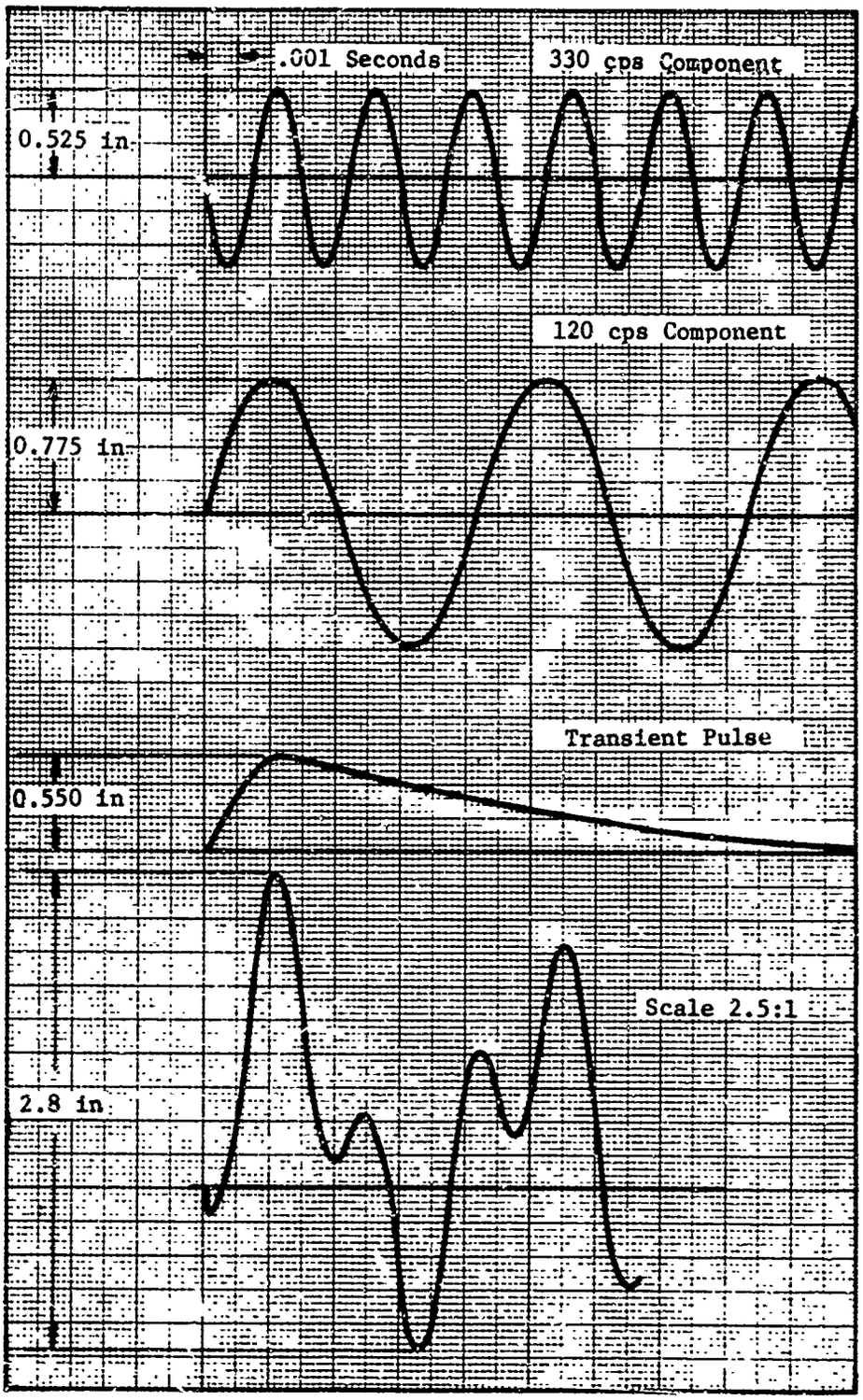

Figure 23

Synthesized Complex Waveform

Model Natural Frequencies of Vibration

Some of the important model natural frequencies of vibration were obtained by tapping on the structure at various locations and recording the output from the accelerometers. This type of frequency survey was considered necessary in order that oscillatory frequencies which occurred during drop testing could be properly evaluated. The results of the frequency survey are presented in Table V. The model was

Table V

Water Impact Model Natural Frequencies of Vibration

Frequency (cps)	Component and Mode
340	Local vertical bending mode of .032 inch thick shell and lower accelerometer
525	Local vertical bending mode of .050 inch thick shell and lower accelerometer
835	Local vertical bending mode of .080 inch thick shell and lower accelerometer
1600	Vertical bending mode involving c. g. accelerometer and bracket
140 700	Coupled vertical response of plate and upper structure

located above the water for this survey. The shell bending frequencies presented involve the local area of the shell near the lower accelerometer. The corresponding vibrations obtained during the drop tests (with the model in the water) were at lower frequencies. The vertical bending response of the c.g. accelerometer and bracket was not present in the test data in view of the filters used. With the lower shells removed, the plate and upper structure of the model exhibited a

coupled response with low damping at approximately 140 and 700 cps. During the tests, with the lower shell fastened to the plate, high responses were obtained at frequencies of 115 cps, 120 cps, and 133 cps corresponding with the installation of 0.032, 0.050, and 0.080 inch thick shells respectively. A frequency of approximately 700 cps was also observed in the test data with the 0.032 inch thick shell installed.

Measured Impact Accelerations

Appendix C presents tabulated results from the data reduction. These results are summarized briefly in the following.

Lower Shell Accelerations. The acceleration responses at the centers of each shell were predominantly in narrow frequency bands which changed for each shell thickness. There were frequency components present in the shell vibrations during the early parts of the impact responses which could not be obtained by visual reduction because of the high levels of response at the shell vibration frequencies. In each test record, the frequency of the shell oscillations could be observed on the trace corresponding to the acceleration at the center of mass. However, in the case of the model with 0.032 inch thick shell, the predominant shell oscillation frequency could not be obtained immediately following impact due to the very complex nature of the response. Also, for this test, there was an additional response frequency at approximately 700 cps in the record which prevented obtaining quantitative results from a visual type analysis. Therefore, complete data reduction was not attempted for the test results from the model with the 0.032 inch thick shell. The shell vibration

frequencies for the models with 0.050 and 0.080 inch thick shells were obtained as average frequencies over the first few cycles following impact. The vibration frequency for the model with the 0.032 inch thick shell was obtained approximately 0.060 - 0.080 seconds after impact. The predominant response frequencies were:

Model Configuration	Shell Vibration Frequency
0.032 inch shell	276 cps
0.050 inch shell	330 cps
0.080 inch shell	400 cps

Since the shells were in the water, the response frequencies indicated above necessarily involved oscillation of some water along with the shell structure. The shell oscillations showed low damping after the first few cycles of vibration. The actual peak accelerations could not be obtained since the records were overloaded during the first few cycles of response.

Center of Gravity Accelerations. The acceleration at the model c.g. for each test involved significant oscillatory components superimposed on the transient rigid body type of response. The phase relationships among the various components were different with the different shells installed on the model. Hence, there was very little correlation in the overall peak responses at any particular time after impact. The peak accelerations obtained were:

Model Configuration	Peak Accelerations
0.032 inch shell	+59.2 peak g overall at 0.026 seconds after impact
	-66.0 peak g overall at 0.03 seconds after impact

Model Configuration	Peak Accelerations
0.050 inch shell	+63.6 peak g overall at 0.003 seconds after impact
0.080 inch shell	+50.0 peak g overall at 0.002 seconds after impact

The above overall peak responses were significantly affected by structural vibrations in the 115 cps - 133 cps frequency range. In view of this, it was necessary to remove these responses by harmonic analyses as previously indicated. The amplitudes of response at 120 cps and 133 cps were removed from the overall recorded c. g. acceleration-time histories for the test results with the 0.050 and 0.080 inch thick shells respectively. The test results for the model with the 0.032 inch thick shell were not analyzed in this manner. The resulting peak accelerations for tests 5 and 6 were:

Model Configuration	Peak Acceleration
0.050 inch shell	34g
0.080 inch shell	28g

Rigid Body Type Accelerations. The peak value of the transient rigid body type response (over the first 0.02 seconds) was obtained during the data reduction for comparison with results from the rigid body theory in Section II. The peak experimental value of this response for the contact velocity of approximately 10 ft/second, averaged over drops 4, 5, and 6, was 18.1g. This peak value was estimated to occur at 0.002 - 0.003 seconds after initial contact with the water. The shape of the rigid body type acceleration-time history could not be accurately obtained. The estimated shape was previously shown in Figure 23.

V. Comparison of Theoretical and Experimental Results

Prior to a discussion of impact accelerations, it should be noted that the peak pressure on the model with the 0.040 inch thick shell was predicted to be 87.9 psi at a contact velocity of 20 ft/sec based on the flexible body theory of Section II (See Appendix B, Table IX). The theoretical pressure-time history indicated that the applied pressure would exceed the calculated critical buckling pressure (35.3 psi) for a short time of about 1.5 milli-seconds. The first two drops were conducted at contact velocities of approximately 20 ft/sec. After the first drop, there were very slight waves in the lower section of the 0.040 shell. After the second drop, this same shell had a large permanent buckle approximately 0.75 inches deep. Subsequent testing was conducted at the reduced contact velocity of 10 ft/sec. No further buckling was encountered although the shell accelerations were considerably higher than expected.

After the experimental program was completed, a very cursory theoretical analysis was conducted to determine the magnitude of the lower shell accelerations based on equations (2.44) and (2.45) in Section II. It was found that the shell accelerations could be several time higher than the c.g. accelerations. Further work with these equations would be desirable in view of the fact that the experimental results showed that the shell accelerations exceeded 200g.

Although this study did not cover the shock wave phase of the water impact phenomena the shock wave pressure on the lower shell would be, by theory, on the order of $\rho c V_o$ where c = the velocity of sound in water (4800 ft/sec). For ρ = 1.94 slugs/ft^3 and V_o = 10 ft/

sec, the pressure would be (equations from References 1 and 2)

$$p = \rho c V_o = 647 \text{ lb/in}^2$$

The duration of this high pressure would be given by

$$t = \frac{RV_o}{2c^2} = 0.435 \times 10^{-6} \text{ seconds}$$

where R is the radius of the shell. Also, since the water in the test tank was approximately 2.5 feet deep, a shock wave would have traveled to the bottom of the tank and returned to the top in approximately one milli-second. The effects, if any, which these factors produced on the experimental results are unknown.

The following sections will present a comparison of the theoretical and experimental acceleration-time histories that were obtained in this study. First, a comparison will be made of important response frequencies and then a comparison will be made of the acceleration levels.

Comparison of Response Frequencies

The theoretical acceleration-time history for a flexible body (see Section II) indicates that the center of mass will undergo an oscillatory response superimposed on the rigid body type of acceleration-time history. Theoretically predicted frequencies of oscillation were obtained by plotting the acceleration data from the computer for the mathematical models with 0.032, 0.050 and 0.080 inch thick shells. For each configuration, the theoretical frequency changes with time; in the following discussion the frequency will be considered as the average frequency which occurs during the first few cycles. Therefore, the simple theoretical model predicts only one frequency or mode of response for each configuration.

The experimental results indicate significant oscillatory responses at more than one frequency because of the large number of degrees of freedom in the experimental model. However, there was a significant frequency of oscillation in the test results for each test configuration which did not correspond to a natural frequency of vibration with the model suspended above the water. For tests with the 0.050 and 0.080 inch thick shells, this frequency was the predominant response frequency for the lower shell immediately after the shell contacted th water. Responses at the same frequencies, were also observed at lower acceleration levels at the model c.g. Table VI compares these experimental frequencies with the theoretically predicted c.g. response frequencies. It can be seen that the theoretical frequencies are about 11 to 25 percent higher than the experimental frequencies. The theoretical frequencies are controlled by the mass of the body and also by the approximations for the shell spring rate and the virtual mass of water. There are insufficient experimental data from the present study to enable separate evaluations of the validity of the approximations.

Table VI

Comparison of Coupled Structural-Water Frequencies of Vibration Obtained from Theoretical and Experimental Investigations

Model Configuration (Shell Thickness) in	Theoretical Vibration Frequency cps	Experimental Vibration Frequency cps
0.032	308	276
0.050	400	330
0.080	500	400

Comparison of Acceleration Levels

Section IV described the data reduction procedure that was used for the model c.g. acceleration records and presented peak acceleration levels obtained from the experiments. Responses at 120 cps and 133 cps were removed from the experimental acceleration-time history data for the 0.050 and 0.080 inch thick shell configurations respectively to enable a quantitative comparison of theoretical and experimental results. The resulting acceleration-time histories for the first 0.005 seconds following initial contact with the water are shown in Figures 24 and 25 for the 0.050 and 0.080 inch thick shell configurations.

It is observed that at time t = 0, the experimental curves start out approximately 180 degrees out of phase from the theoretical curves. This negative peak (actually a positive downward acceleration) was observed in the test records for all the different shell configurations. Therefore, the experimental data have been plotted with the same initial phase relationships that were obtained from the tests. However, in the harmonic analysis of the data and in the removal of components, it was necessary to assume phase relationships among the frequency components in each record. Therefore, the phasing in the experimental data following time t = 0 is subject to error. This possible error in phasing did not appear to significantly affect the peak accelerations. The experimental acceleration time-histories shown in Figures 24 and 25 exhibit peak values which are about the same as the sums of the individual components.

The reason for the initial downward acceleration at the model c.g., as shown in the experimental data, is not entirely known. In the experimental model, the shells were fastened to beveled edges of

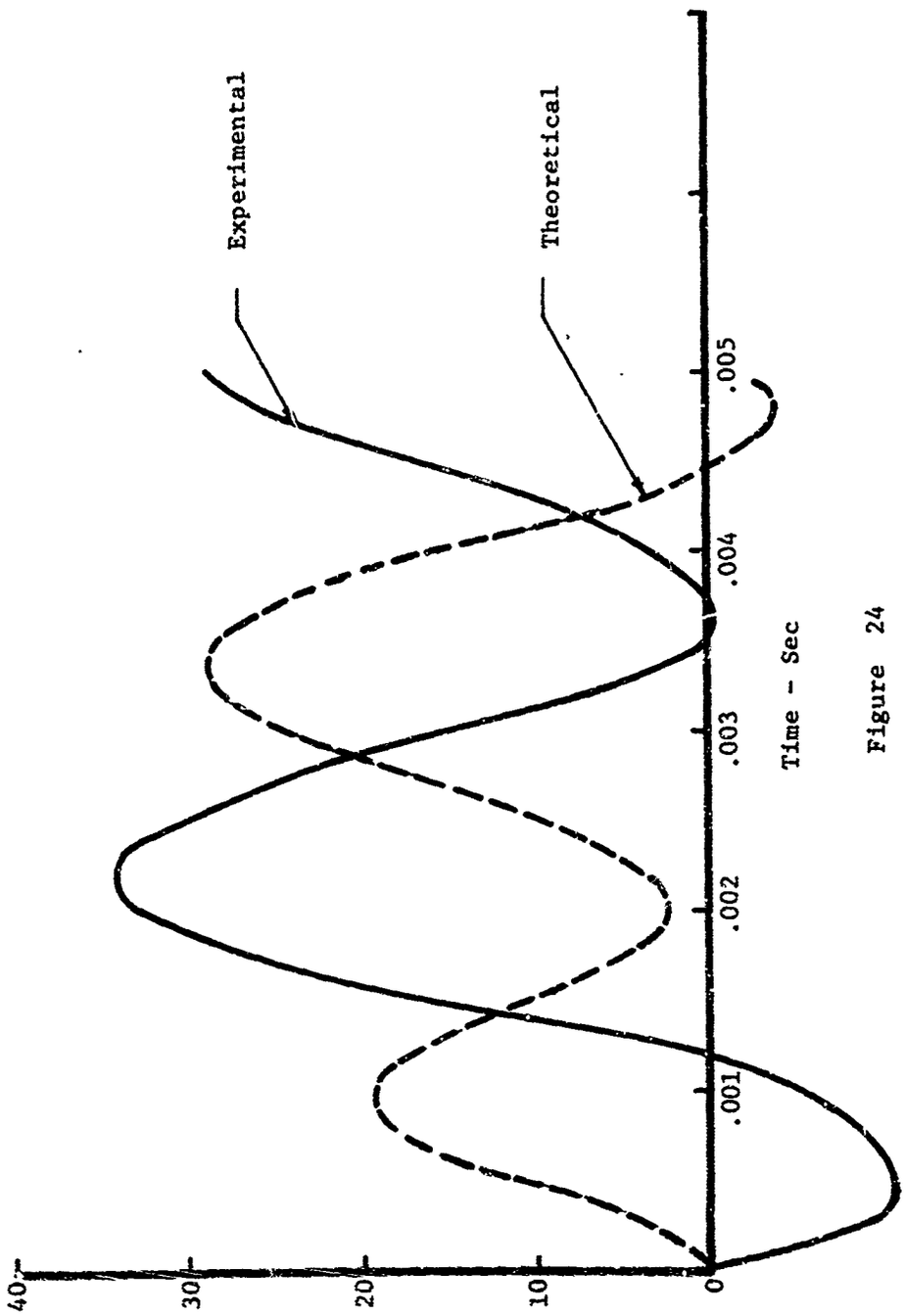

Figure 24

Comparison of Acceleration-Time Histories Obtained from Theoretical Investigation and Model Test (Data from Model with 0.050 Inch Thick Spherical Shell)

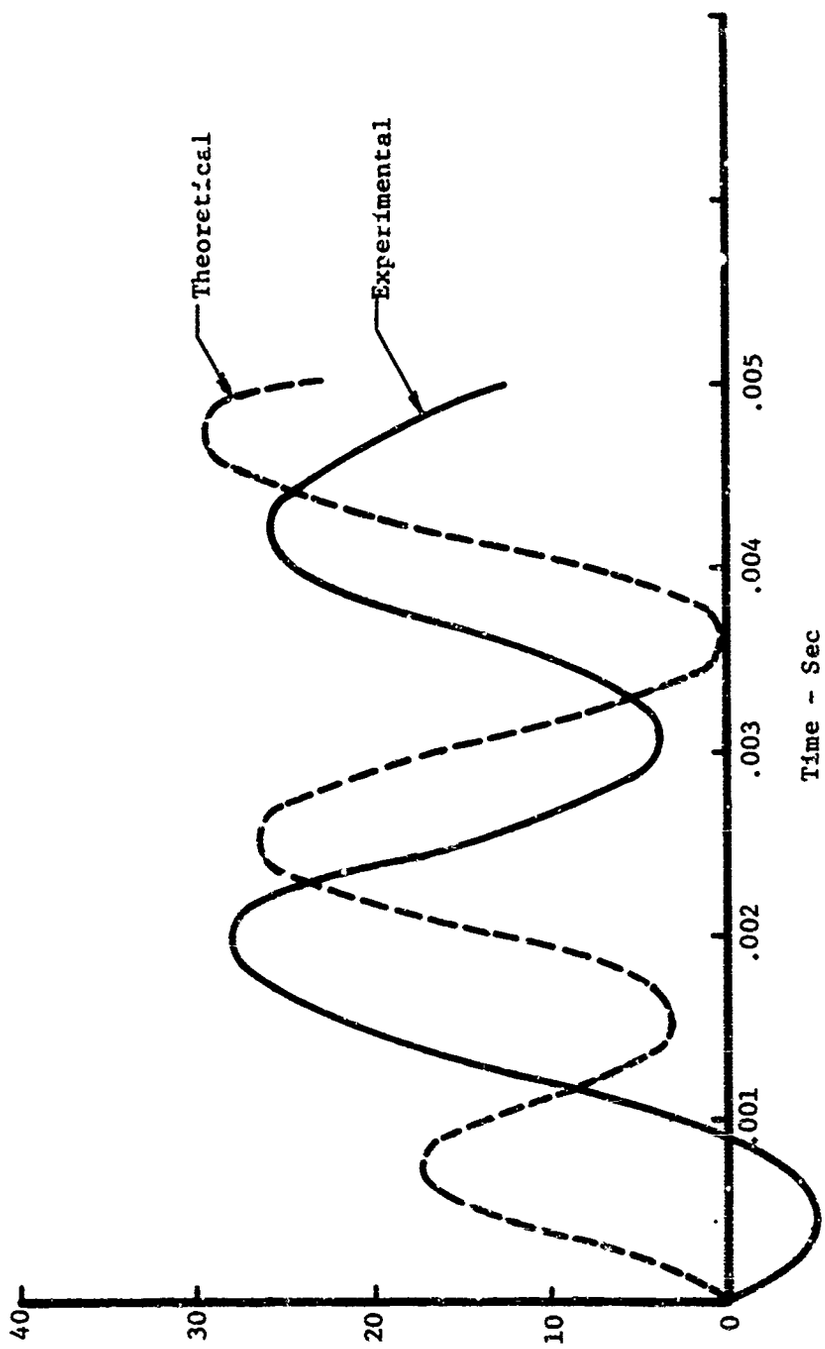

Figure 25

Comparison of Acceleration-Time Histories Obtained from Theoretical Investigation and Model Test (Data from Model with 0.080 Inch Thick Spherical Shell)

an aluminum plate and the c.g. accelerometer was mounted on a stiff bracket at the center of the plate. It is believed that the strong initial upward impact load at the outer edge of the plate caused the plate to bend with an initial downward motion at the center of the plate.

Theoretical acceleration-time histories for V_o = 10 ft/sec, R = 24 inches, and W = 30 lbs, which correspond approximately to the test conditions, are shown in Figures 24 and 25 for the first 0.005 seconds following initial contact with the water. The total time interval over which the theoretical results could be considered valid may be beyond 0.005 seconds, but the theory used did not consider several forces, including bouyancy, which would limit the range over which the theoretical results would be valid.

The peak values of acceleration from the experimental acceleration-time histories are compared below with the peak theoretical values which occurred during the 0.002 - 0.004 second time interval following time t = 0. The average of the theoretical peak values was approximately 10 percent below the average of the experimental peak values.

Model Configuration	Theoretical Peak Acceleration	Experimental Peak Acceleration
0.050 inch shell	29g	34g
0.080 inch shell	26.5g	28g

The theoretically predicted rigid body acceleration-time history for V_o = 10 ft/sec, R = 24 inches, and W = 30 lb is shown in Figure 26. A peak value of 14.38g occurred 0.003 seconds after contact with the water. The average value of the peak rigid body type acceleration (18.1g) which was obtained from the experiments is also shown in

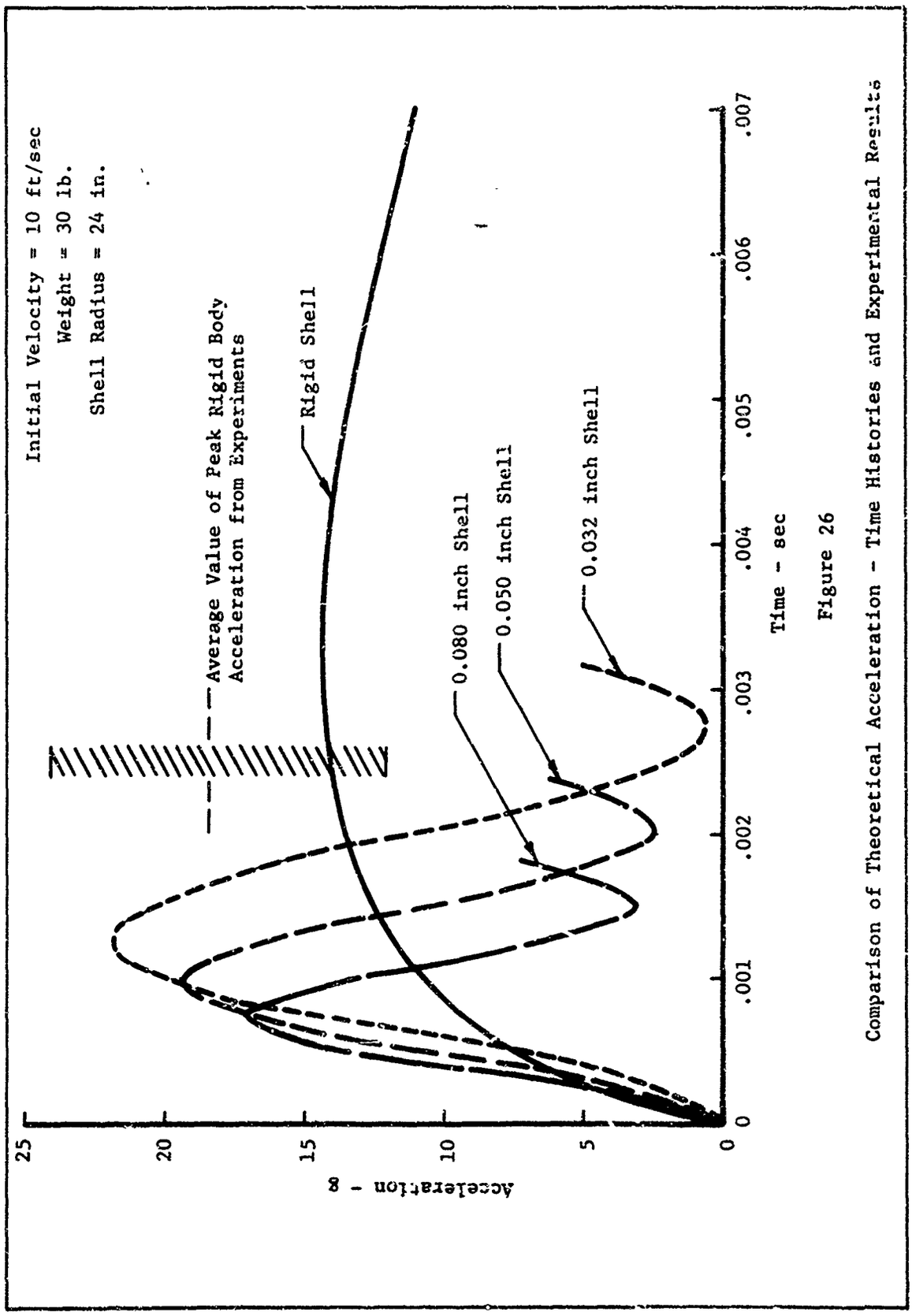

Figure 26

Comparison of Theoretical Acceleration - Time Histories and Experimental Results

Figure 26. The peak experimental value was estimated to occur at 0.002 to 0.003 seconds after contact with the water. Although peak experimental values obtained from the data reduction ranged only from 16g to 20.8g, a wider range of possible error is shown in Figure 26 by the dashed lines. Figure 26 also shows the first peaks in the theoretical acceleration-time histories for the center of mass of flexible structures. These curves illustrate the manner in which a change of spring stiffness in the theoretical model will cause corresponding changes in levels and frequencies of the dynamic responses.

VI. Conclusions

1. The theoretical developments of Section II for a flexible structure provide a means for predicting dynamic interactions among inertial, elastic and hydrodynamic forces during water impact. However, the present theoretical model is relatively simple and considers only the flexibility of spherical shell structures. The applicability of the theory to more realistic complex structures would require additional study.

2. Dynamic magnifications of response and acceleration at the center of mass, associated with the flexibility of the spherical under surface, are predicted by the theoretical model. Since actual structures are flexible, it is believed that the theoretical model developed in this study provides more accurate predictions of acceleration than the rigid body theory. Measured and predicted accelerations associated with flexible 0.050 and 0.080 inch thick shells were on the order of 30g whereas the predicted peak acceleration from rigid body theory was approximately 14g. This study was limited primarily to the prediction of relative deflections of the spherical shell and the accelerations of the center of mass. Additional studies of the acceleration of the lower shell and virtual mass of water are required for a complete understanding of the theoretical model.

3. Qualitative aspects of the theoretical and experimental results compare favorably. One of the more significant aspects of the results was that predicted coupled responses of the flexible body and a virtual mass of water were also observed in the experimental results. This qualitative correlation of results suggests that the simple theory

presented in Section II may provide an acceptable approach for future theoretical developments which are applicable to more complex systems.

4. In general, the experimental and theoretical results compare favorably on a quantitative basis. The theoretically predicted response frequencies were approximately 20 percent higher than the experimental values. The theoretically predicted acceleration levels for the flexible bodies were about 10 percent lower than the experimentally obtained values. However, the larger number of degrees of freedom in the experimental model, and the attendant complications in the data reduction, limit the accuracy of a quantitative comparison of acceleration levels. Additional test results with an improved model are needed for a more accurate comparison of results and for future improvements in the theory.

VII. Recommendations

The following recommendations are presented:

1. The analyses should be extended to examine acceleration-time histories from equations (2.44) and (2.45) using the Runge-Kutta method presented in Appendix B.

2. Additional testing should be conducted with a modified model, perhaps with a fiberglass upper section, which is quite stiff, to obtain better experimental data which can be compared directly with theoretical results.

3. Results from the theoretical model should be checked on a quantitative basis and an evaluation should be made of the validity of the approximations in the theory.

4. The theory developed in Section II should be extended to cover other structural shapes. Also, an extension of the theory into matrix form would enable the prediction of impact loads in more complex structural configurations.

Bibliography

1. Mosteller, G. G. Water-Entry Acceleration an Annotated Bibliography. NAVORD Report 5397, China Lake, California: 19 December 1956.

2. Collopy, F. H., "Determination of the Water Impact Shock Environment". The Shock and Vibration Bulletin Nr. 35, Part 7: 77-86, Washington, D. C.: U. S. Naval Research Laboratory, April 1966.

3. Von Karman, T. The Impact on Seaplane Floats During Landing. NACA TN 321. Washington: National Advisory Committee for Aeronautics, October 1929.

4. Benson, Harold E. "Water Impact of the Apollo Spacecraft". Journal of Spacecraft and Rockets, Vol 3, Nr. 8:1282-1284, August 1966.

5. McGhee, John R., et al. Water-Landing Characteristics of a Reentry Capsule. NASA Memo 5-23-59L. Washington: National Aeronautics and Space Administration, June 1959.

6. Bisplinghoff, R. L. and C. S. Doherty. A Two-Dimensional Study of the Impact of Wedges on a Water Surface. Contract Nr. NOa(s) 9921, Boston, Massachusetts: Dept. Aero Eng., Massachusetts Institute of Technology, March 20, 1950.

7. Hoover, W. R. and P. J. Reardon. Approximate Impact Drag Coefficients for the Vertical Water-Entry of Families of Cone, Ellipsoidal, and Tangent Ogive Nosed Missiles. NOLTR 64-110. White Oak, Maryland: U. S. Naval Ordnance Laboratory, 2 October 1964.

8. Lamb, H. Hydrodynamics (Sixth Edition). New York: Dover Publications, 1945, pp. 123-125.

9. Timoshenko, S. and S. Woinowsky-Krieger. Theory of Plates and Shells (Second Edition). New York: McGraw-Hill Book Company, Inc., 1959, pp. 488-561.

10. Wallace, C. D., Jr. Matrix Analysis of Axisymmetric Shells Under General Loading. AFIT Thesis GAM/MC/66B-7: May 1966.

11. Timoshenko, S. Theory of Elastic Stability. New York: McGraw-Hill Book Company, Inc., 1936, pp. 491-497.

12. Baker, Wilfred E., and Peter S. Westine. "Model Tests for Determination of the Structural Response of the Apollo Command Module to Water Impact". Journal of Spacecraft and Rockets Vol 4, Nr. 2:201-208, February 1967.

Appendix A

Theoretical Data on Rigid Body Water Impact Loads

Method of Analysis

For the Rigid Body studies, equation (2.8) was programmed on the 1620 digital computer using finite difference techniques. Equation (2.8) is repeated below:

$$\dot{y} = \frac{V_o}{1 + \frac{\pi\rho R^3}{2M}\left(\frac{2y}{R} - \frac{y^2}{R^2}\right)^{3/2}} \tag{2.8}$$

The Δt time increment used was 0.00025 seconds for the first ten time intervals. This time increment was then increased to 0.00050 seconds for the second ten time intervals. Larger time intervals of 0.001 and 0.002 seconds were also used for the later stages of motion of a rigid body since rates of changes were not very large.

Table VII shows an example of the theoretical data obtained. Normally, the programs were run for 40 time increments. The radius of the sphere, R, weight, W, and initial (contact) velocity, V_o, were input data for the computer program. The constant for the virtual mass to structural mass ratio was

$$C = \frac{\pi\rho g R^3}{2W} \tag{A.1}$$

where $\rho g = 62.5\ lb/ft^3$

In addition to obtaining velocity increments, as defined by equation (2.8), the output included the following:

$$\sin\phi = \left(\frac{2y}{R} - \frac{y^2}{R^2}\right)^{1/2} \tag{A.2}$$

Table VII

Rigid Body Water Impact Loads

t sec	Δy ft	y ft	sin ϕ	$\dot{y}$ ft/sec	$\Delta\dot{y}$ ft/sec	Acceleration g	Force lb	Pressure psi
.00025	.00500	.00500	.07067	19.817	.183	32.743	682.29	75.50
.00050	.00495	.00995	.09965	19.495	.322	39.988	1199.65	66.77
.00075	.00487	.01483	.12154	19.102	.393	48.815	1464.46	54.78
.00100	.00478	.01960	.13967	18.668	.434	53.870	1616.11	45.78
.00125	.00467	.02427	.15532	18.213	.455	56.516	1695.47	38.84
.00150	.00455	.02882	.16916	17.750	.463	57.516	1725.47	33.32
.00175	.00444	.03326	.18162	17.289	.462	57.378	1721.35	28.84
.00200	.00432	.03758	.19295	16.834	.455	56.462	1693.86	25.14
.00225	.00421	.04179	.20336	16.391	.443	55.025	1650.76	22.06
.00250	.00410	.04589	.21299	15.962	.429	53.255	1597.66	19.46
.00300	.00798	.05387	.23053	15.143	.819	50.900	1527.01	15.88
.00350	.00757	.06144	.24597	14.393	.750	46.582	1397.47	12.77
.00400	.00720	.06864	.25973	13.711	.682	42.378	1271.34	10.41
.00450	.00686	.07549	.27216	13.091	.619	38.477	1154.30	8.61
.00500	.00655	.08204	.28347	12.529	.563	34.946	1048.37	7.21
.00550	.00626	.08830	.29386	12.017	.512	31.791	953.73	6.10
.00600	.00601	.09431	.30346	11.550	.467	28.990	869.70	5.22
.00650	.00577	.10009	.31238	11.123	.427	26.509	795.28	4.50
.00700	.00556	.10565	.32072	10.732	.391	24.313	729.38	3.92
.00750	.00537	.11101	.32853	10.372	.360	22.365	670.96	3.44

$$\Delta\dot{y} = \dot{y}_i - \dot{y}_{i+1} \text{ (expressed as positive)} \quad (A.3)$$

$$\text{Acceleration (g)} = \Delta\dot{y}/(\Delta t \times 32.2) \quad (A.4)$$

$$\text{Force} = W \times \text{Acceleration (g)} \quad (A.5)$$

$$\text{Pressure} = \text{Force} / [144 \times \pi \times (R \sin \phi)^2] \quad (A.6)$$

The input data for Table VII was:

$R = 2$ ft

$W = 30$ lb

$V_o = 20$ ft/sec

Summary of Theoretical Data

Table VIII presents a summary of theoretical data for the rigid sphere entering water. Results were obtained from computer runs for 8 variations in the input data. The values of peak acceleration and force presented correspond to the maximum values obtained from the computer output sheets. The values of pressure presented correspond to the first Δt time interval since these were the highest values obtained for rigid bodies.

The peak accelerations presented in Table VIII are also shown in Figure 27 along with a basic curve for R = 20 ft/sec, W - 30 lb, and V_G = 20 ft/sec. Two of the three input variables always correspond to those for the basic curve. The value of the third variable is indicated in Figure 27.

If curves were plotted for each of the 8 variations in input, the general shape of each acceleration-time history would be similar to the basic curve shown except that the peak acceleration would occur at the respective point indicated in Figure 27. Curves have been added to show trends due to separate changes in the three variables. These data were obtained in the present study primarily as an aid for the selection of model weight and shell radius for the experimental part of the study.

Table VIII

Summary of Theoretical Data for Rigid Sphere Entering Water

Radius (ft)	Contact Velocity (ft/sec)	Weight (lb)	Peak Acceleration (g)	Time to Reach Peak Acceleration (sec)	Maximum Force (lb)	Pressure at 0.00025 sec. (psi)
1.0	20	30	27.55	.00300	826.57	53.67
1.5	20	30	42.57	.00200	1276.98	65.59
2.0	20	30	57.52	.00150	1725.47	75.50
2.5	20	30	72.51	.00125	2175.42	84.12
2.0	10	30	14.38	.00300	431.30	26.86
2.0	30	30	129.84	.00100	3895.10	137.61
2.0	20	15	92.41	.00100	1385.11	74.82
2.0	20	60	35.80	.00250	2147.74	75.85

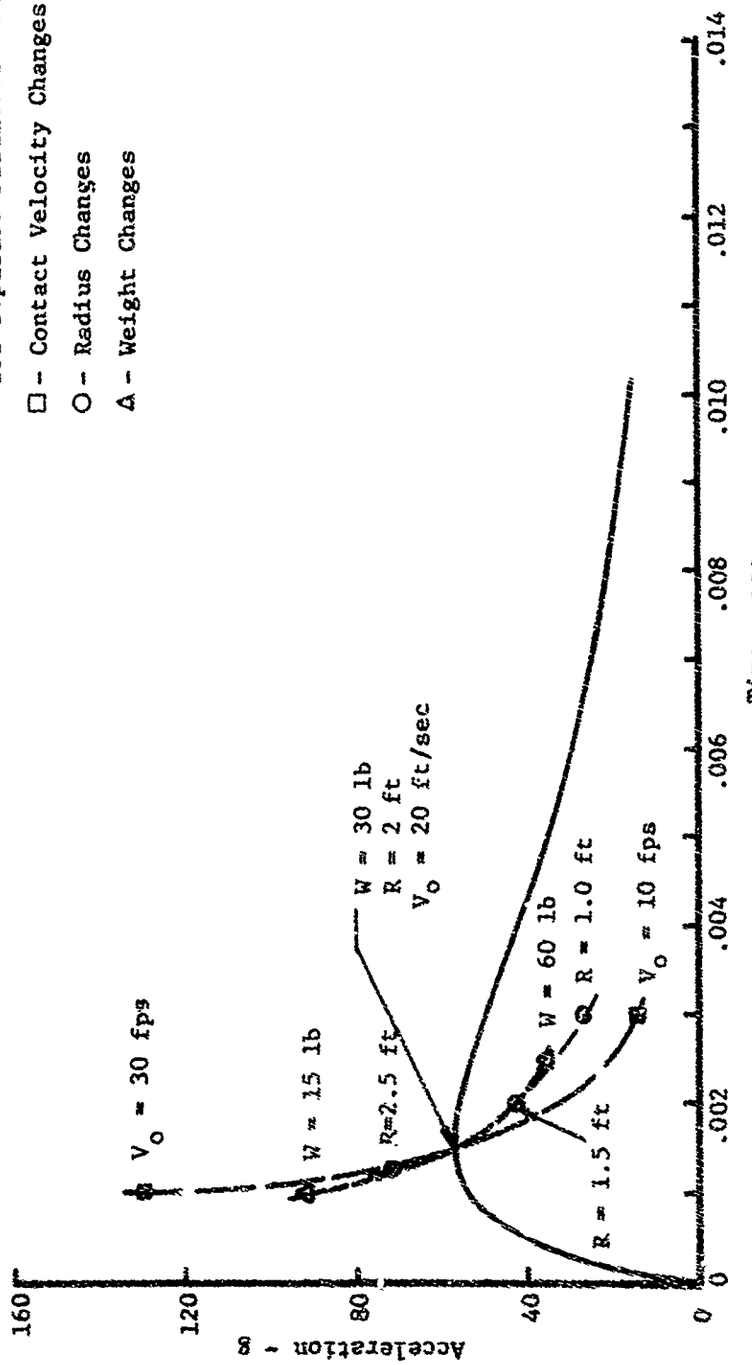

Figure 27

Variations in Peak Accelerations Corresponding to Changes In Contact Velocity, V_o, Radius, R, and Weight, W, for A Rigid Sphere Entering Water

Effects of Changing the Virtual Mass

In the foregoing discussion, the constant in the analytical expression for the virtual mass to structural mass ratio was

$$C = \frac{\pi \rho g R^3}{2W}$$

However, much of the literature on water impact loads considers the constant as

$$C_1 = \frac{4 \rho g R^3}{3W}$$

For the following conditions:

$$R = 2 \text{ ft}$$

$$W = 30 \text{ lb}$$

$$\rho g = 62.5 \text{ lb/ft}^3$$

the values of these constants are:

$$C = 26.18$$

$$C_1 = 22.22$$

An additional computer run was made (V_o = 20 ft/sec) using the value C_1 in the expression for the virtual mass. The resulting acceleration-time history is shown in Fig 28. The peak acceleration was reduced by 10.5 percent as a result of this change in the constant.

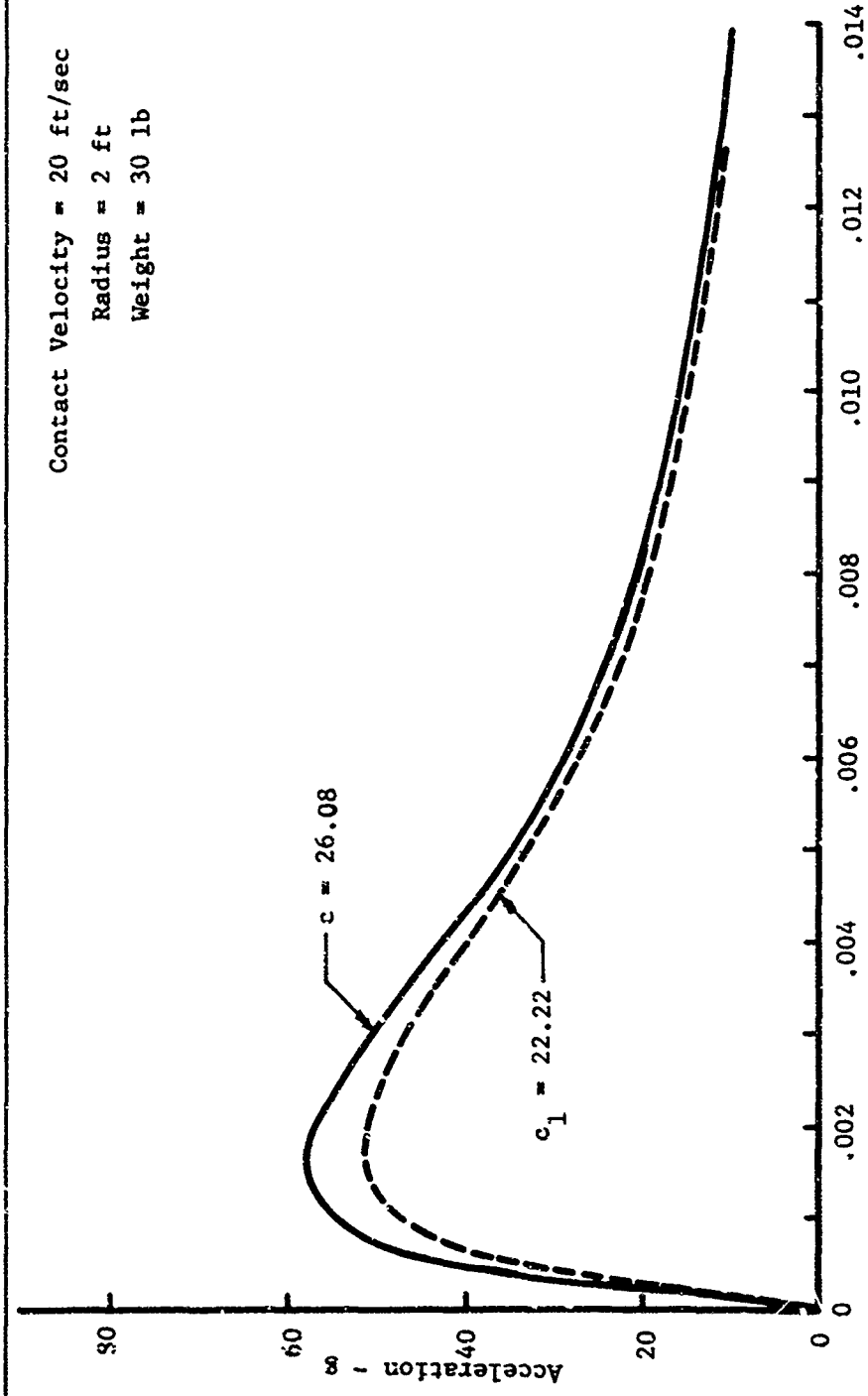

Figure 28

Comparison of Theoretical Acceleration-Time Histories for Two Values of the Constant in the Expression for the Virtual Mass of Water

Appendix B

Theoretical Data on Flexible Body Water Impact Loads

Deflections of Thin Spherical Shell Segments

In Section II, the momentum equation (2.18) contained the fraction, χ, which reduced the shell center deflection velocity to some effective vertical velocity over the deflected portion of the shell. Figure 29 shows approximate deflection shapes for a thin aluminum shell segment 0.040 inch thick which were obtained from the Matrix Analysis Program of Reference 10. The shell geometry and loading angle ϕ were shown in Section II, Figure 10 and the shell center deflections were presented in Table III for various applied pressures. For the deflections shown in Figure 29, the applied pressure was 100 psi in each case; these deflections correspond to linear theory only (no buckling was considered). It can be seen that the shell deformation is fairly local (i.e. it does not extend appreciably beyond the edge of the applied load).

An approximate value for the average deflection over the area of the applied pressure loading may be obtained from the following simplifying assumptions:

Assume the deflection varies linearly from δ_o at the center to $\delta_o/2$ at the edge of the applied loading. Then the deflection along the projected radius is expressed by

$$\delta(r) = (1 - \frac{x}{2r})\ \delta_o$$

and

$$\delta(\text{area}) = \frac{1}{\pi r^2} \int_0^r 2\pi x \delta_o\ (1 - \frac{x}{2r}) dx \qquad \text{(B.1)}$$

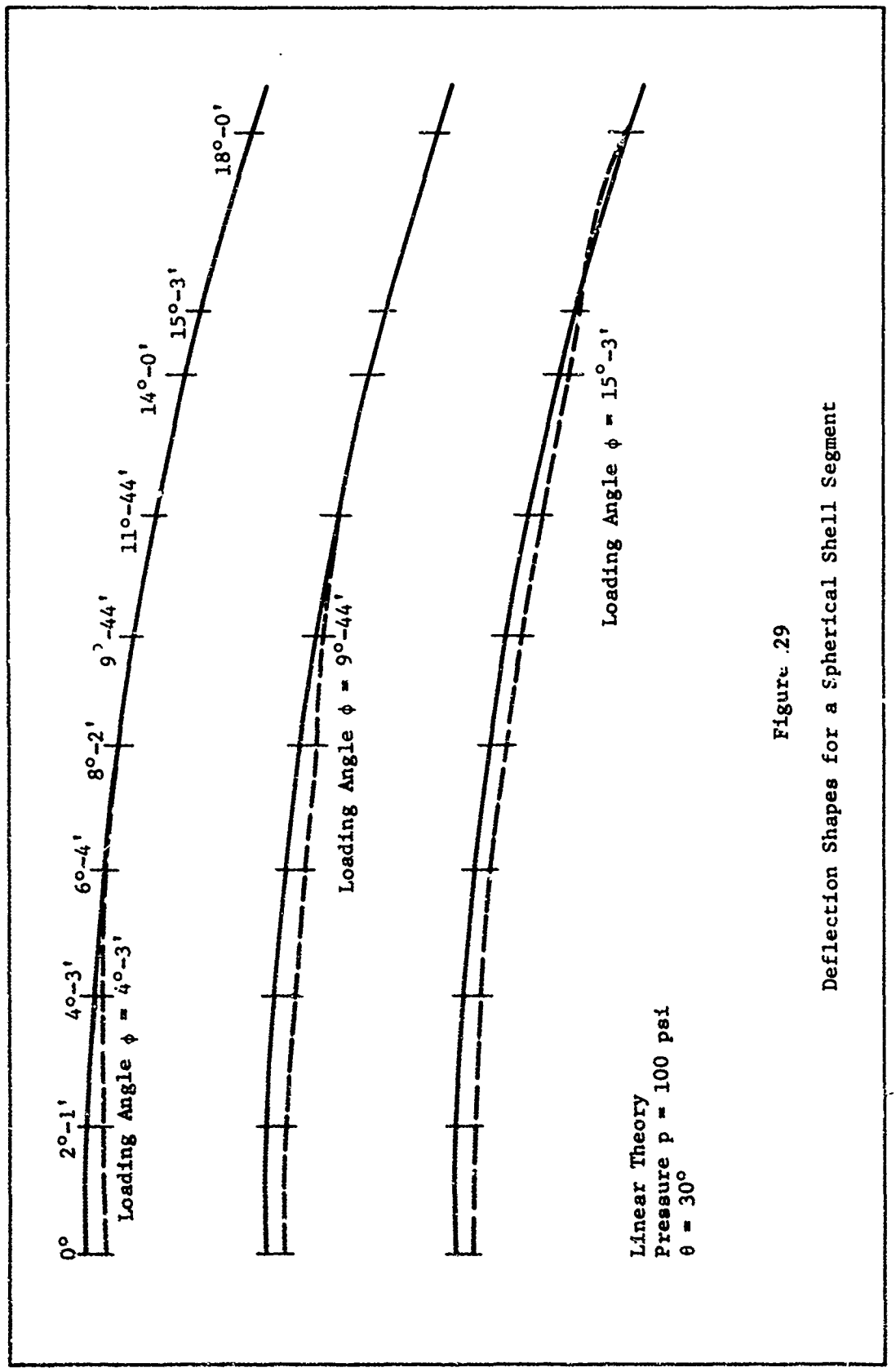

Figure 29

Deflection Shapes for a Spherical Shell Segment

$$\delta(\text{area}) = \frac{2\delta_o}{r^2} \left[\frac{r^2}{2} - \frac{r^2}{6} \right]$$

$$\delta(\text{area}) = \frac{2}{3} \delta_o$$

Other analytical expressions for the average deflection, perhaps more exact, could be developed based on the deflection shapes indicated in Figure 29. However, the deflection shape under dynamic loading may also be different than the curves of Figure 29 which apply for static loading.

Solution of a Set of Simultaneous Ordinary Differential Equations By The Runge-Kutta Method

The Runge-Kutta program solves a set of first order differential equations of the form

$$\frac{dy_i}{dt} = F_i\ (t, y_1, y_2, \ldots, y_n)\ i = 1, 2, \ldots, n$$

A differential equation of higher order can be expressed as a set of first order equations by a change of variables. For the standard program used in this study, the variables on the left sides of the above statements were F(1), . . ., F(3) and the right sides contained the subscripted variables y(1), . . ., y(3).

Equations (2.42) and (2.43) from Section II were put into Runge-Kutta format as follows:

$$\dot{y}_1 = \frac{V_o + \frac{m^*}{M} \dot{\delta}_o}{1 + \frac{m^*}{M}} \qquad (2.42)$$

$$\ddot{y}_1 = -\frac{K}{M} \delta_o \qquad (2.43)$$

Let: $\dot{y}_1 = y_2$ (change in variables)

$\delta_o = y_3$

Then equations (2.42) and (2.43) can be written as

$$\dot{y}_1 = F(1) = y(2) \tag{B.2}$$

$$\dot{y}_2 = F(2) = -\frac{K}{M}\ y(3) \tag{B.3}$$

$$\dot{y}_3 = F(3) = \frac{M}{m^*}\left[\left(1 + \frac{m^*}{M}\right)\ y(2) - V_o\right] \tag{B.4}$$

where, from Section II,

$$K = \pi\ E\ h\left(\frac{2y(1)}{R} - \frac{y(1)^2}{R^2}\right)$$

$$m^* = \frac{\pi\rho R^3}{2}\left(\frac{2y(1)}{R} - \frac{y(1)^2}{R^2}\right)^{3/2}$$

In the Runge-Kutta program, initial values were assigned to t, y(1), y(2), and y(3). In the present study, the actual initial values were:

$t = 0$

$y(1) = 0$

$y(2) = V_o$

$y(3) = 0$

However, with these initial conditions, equation (B.4) above has the indeterminant form 0/0. Therefore, y(1) was given a very small value of 1×10^{-6} to start the program.

An example of the output from the Runge-Kutta program is shown in Table IX. Normally the program output is t, y(1), . . ., y(n). The program was modified to obtain c.g. acceleration, force, and

Table IX

Runga-Kutta Solution For Differential Equations

t sec	y_1 ft	$\dot{y}_1$ ft/sec	δ_o ft	$\ddot{y}_1$ ft/sec^2	Force lb	Pressure lb/in^2
0.00000	.0000010	20.00000	0.0000000	0.0000	0.000	0.000
.00025	.0049993	19.97082	.0042931	11.3278	339.833	37.565
.00050	.0099715	19.76987	.0077597	40.8385	1225.154	67.898
.00075	.0148607	19.29970	.0096794	75.9192	2277.577	84.696
.00100	.0195985	18.56770	.0100486	103.9431	3118.292	87.927
.00125	.0241301	17.67094	.0090846	115.6985	3470.956	79.491
.00150	.0284324	16.75973	.0071547	107.3668	3221.005	62.604
.00175	.0325219	15.99138	.0047176	80.9765	2429.296	41.279
.00200	.0364505	15.48622	.0022562	43.4065	1302.194	19.742
.00225	.0402919	15.29629	.0002049	4.3576	130.727	1.793
.00250	.0441231	15.39239	-.0011207	-26.0991	-782.973	-9.806
.00275	.0480038	15.67073	-.0015727	-39.8468	-1195.403	-13.761
.00300	.0519610	15.97639	-.0011868	-32.5464	-976.393	-10.384
.00325	.0559800	16.13869	-.0001601	-4.7307	-141.922	-1.401
.00350	.0600059	16.01177	.0012004	38.0189	1140.566	10.504
.00375	.0639543	15.51234	.0025471	85.9762	2579.287	22.287
.00400	.0677308	14.64566	.0035606	127.2830	3818.489	31.155
.00425	.0712542	13.51166	.0040092	150.7779	4523.337	35.081
.00450	.0744787	12.28720	.0037896	148.9676	4469.029	33.159
.00475	.0774081	11.18681	.0029431	120.2435	3607.305	25.753
.00500	.0800994	10.41125	.0016463	69.5990	2087.971	14.405

pressure. Although the initera force would be negative, the output equations were arranged so that the loads would start out positive. The conditions for Table IX were:

$$V_o = 20 \text{ ft/sec}$$

$$R = 2 \text{ ft}$$

$$W = 30 \text{ lb}$$

$$h = 0.04/12 \text{ ft.}$$

$$E = 144 \times 10.5 \times 10^6 \text{ lb/ft}^2$$

$$\rho g = 62.5 \text{ lb/ft}^3$$

The programs were run with time increments of 0.00025 seconds for a total time of 0.015 seconds.

Equations (2.44) and (2.45), Section II, were also put into the standard Runge-Kutta format to check the deflection-time history. The equations used are indicated in the following:

$$\dot{y}_2 = \frac{M}{m^*} (V_o - \dot{y}_1) \tag{2.44}$$

$$\ddot{y}_2 = \frac{1}{m^*} \left[K (y_1 - y_2) - \dot{m}^* \dot{y}_2 \right] \tag{2.45}$$

where y_2 is the coordinate at the lower center of the shell. This is not the same as the change in variable previously indicated. For equations (2.44) and (2.45), let:

$$\dot{y}_2 = y_3$$

Then

$$\dot{y}_1 = F(1) = V_o - \frac{m^*}{M} y(3) \tag{B.5}$$

$$\dot{y}_2 = F(2) = y(3) \tag{B.6}$$

$$\dot{y}_3 = F(3) = \frac{1}{m^*} \left[K \left(y(1) - y(2) \right) - \dot{m}^* \dot{y}(2) \right] \tag{B.7}$$

Where K and m* are the same as in the previous equations and

$$\dot{m}^* = \frac{3\pi\rho R^2}{2}\left(\frac{2y(1)}{R} - \frac{y(1)^2}{R^2}\right)^{1/2}\left(1 - \frac{y(1)}{R}\right)\dot{y}(1) \quad (B.8)$$

The output from the above equations yielded values for y(1) and y(2) from which the relative deflection, δ_o, could be obtained. Table X presents a comparison of results from the two sets of differential equations. The initial values for y(1), y(2) and y(3) in equations (B.5) through (B.7) were:

$$y(1) = 1 \times 10^{-6}$$

$$y(2) = 1 \times 10^{-6}$$

$$y(3) = 0$$

The structural parameters and initial contact velocity were the same as those indicated for Table IX.

In order to evaluate the effects of changing the shell thickness, and hence the spring rate K, additional computer runs were made for 0.032, 0.050, and 0.080 thick shells. The initial contact velocity was 10 ft.sec to provide data which could be compared with the experimental results (See Figure 26, Section V).

An additional study was made for a thick shell to determine whether the equations for a flexible structure would converge to the rigid body results when the spring became very stiff. A spring stiffness corresponding to a shell 0.25 inches thick was used. The resulting acceleration-time history is shown in Figure 30. An average frequency of oscillation of 800 cps was obtained. However, the time increment used (0.00025 seconds) provided only an average of 5 data points per cycle which was not adequate to completely define the peaks

Table X

Comparison of Relative Deflections As Obtained From the Structural Inertia Force and the Hydrodynamic Reaction Force

t sec	$\delta_o^{(1)}$ ft	$\delta_o^{(2)}$ ft
0	0	0
.00025	.0042931	.0048310
.00050	.0077597	.0081303
.00075	.0096794	.0098595
.00100	.0100486	.0100586
.00125	.0090846	.0089684
.00150	.0071547	.0069685
.00175	.0047176	.0045195
.00200	.0022562	.0020967
.00225	.0002049	.0001186
.00250	-.0011207	-.0011196
.00275	-.0015727	-.0014912
.00300	-.0011868	-.0011491

(1) - Values obtained from Equations (2.42) and (2.43)

(2) - Values obtained from Equations (2.44) and (2.45)

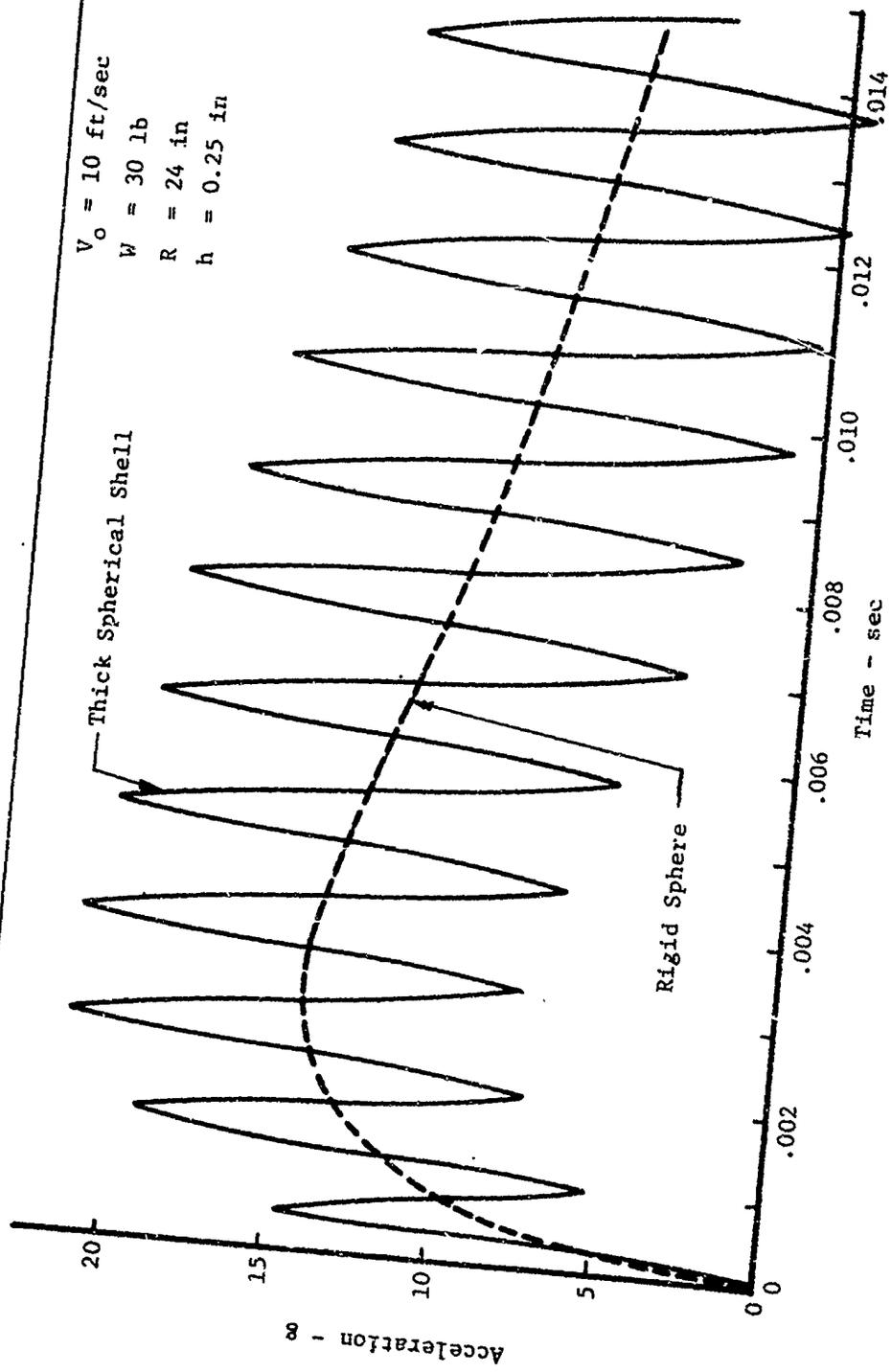

Figure 30

Comparison of Acceleration-Time Histories For A Rigid Sphere and A Thick Spherical Shell

of the curve. The curve in Figure 30 was obtained by constructing approximate sine waves through the data points. It appears that the peak to peak acceleration may continue to increase with time and that a small amount of damping would be desirable in the flexible body equations.

Appendix C

Experimental Data on Flexible Body Water Impact Loads

The experimental data obtained in this study were recorded on tape and on a direct reading oscillograph (visicorder). The visicorder results (oscillograms) were reduced for the analyses presented in Sections IV and V. Since there were structural responses in the test model which produced a rather complex waveform, it was necessary to reduce the data by making an harmonic analysis of each record. Figures 31, 32, and 33 shows tracings of the complex waveforms for drop tests 4, 5, and 6 respectively. The visicorder that was used for these records was operated at a nominal paper speed of 80 inches per second. Timing lines on the records were 0.001 seconds apart. The calibration constant for these data was 80g (peak)/inch film amplitude.

Tables XI, XII, and XIII present the detailed results obtained from the visual harmonic analysis of the records.

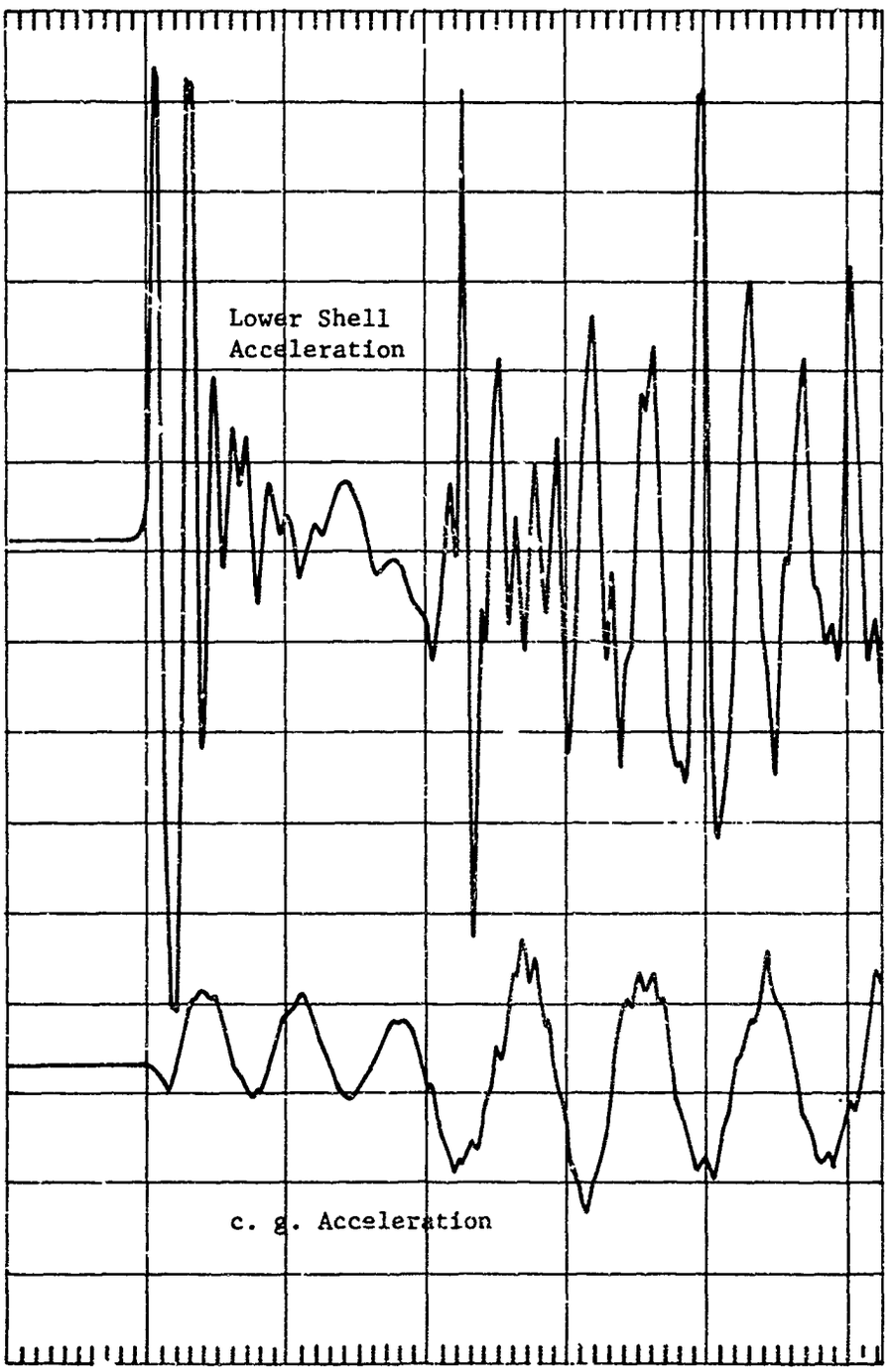

Figure 31

Tracing of Acceleration Record for Model with 0.032 Inch Thick Shell

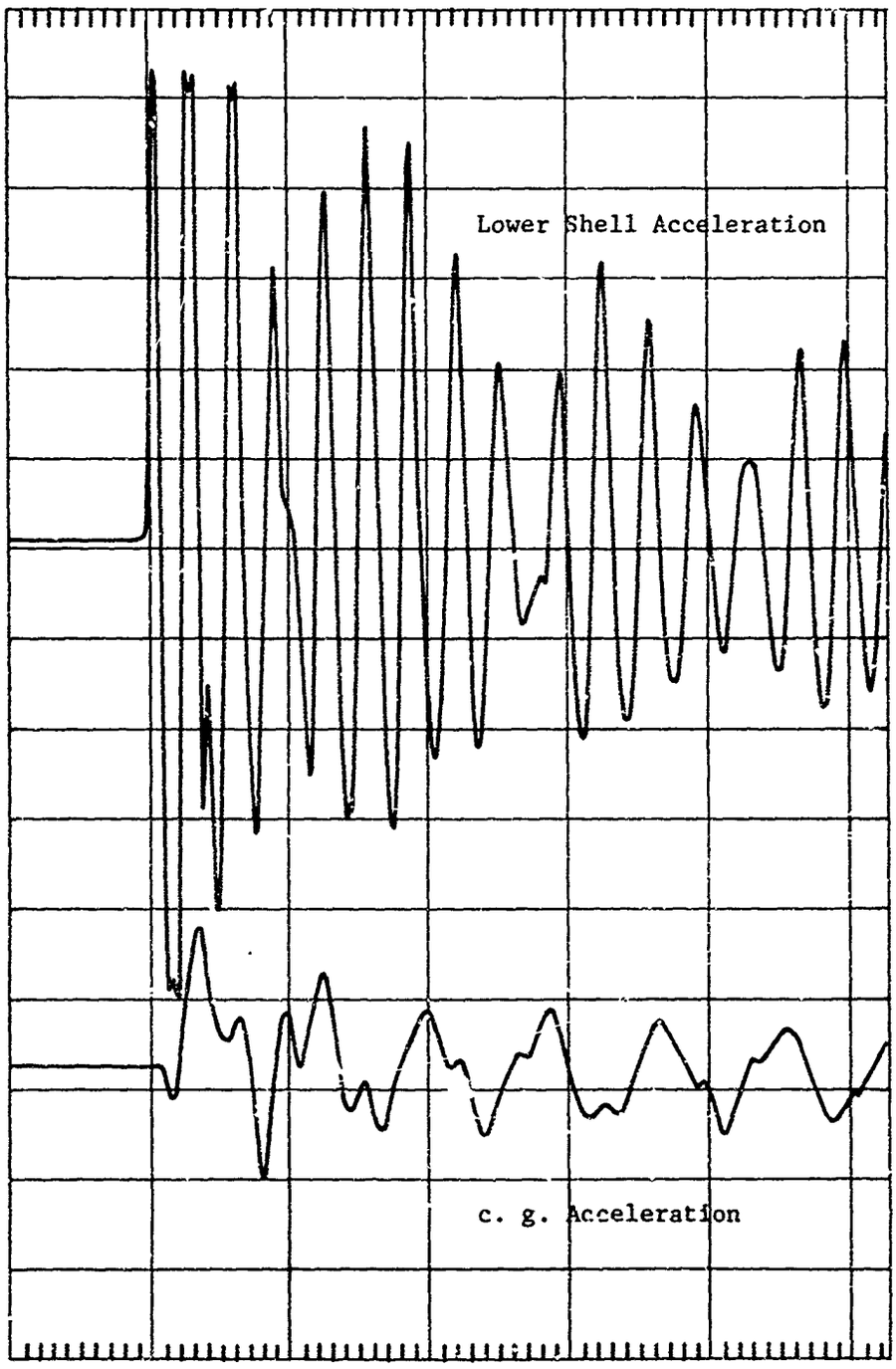

Figure 32

Tracing of Acceleration Record for Model with 0.050 Inch Thick Shell

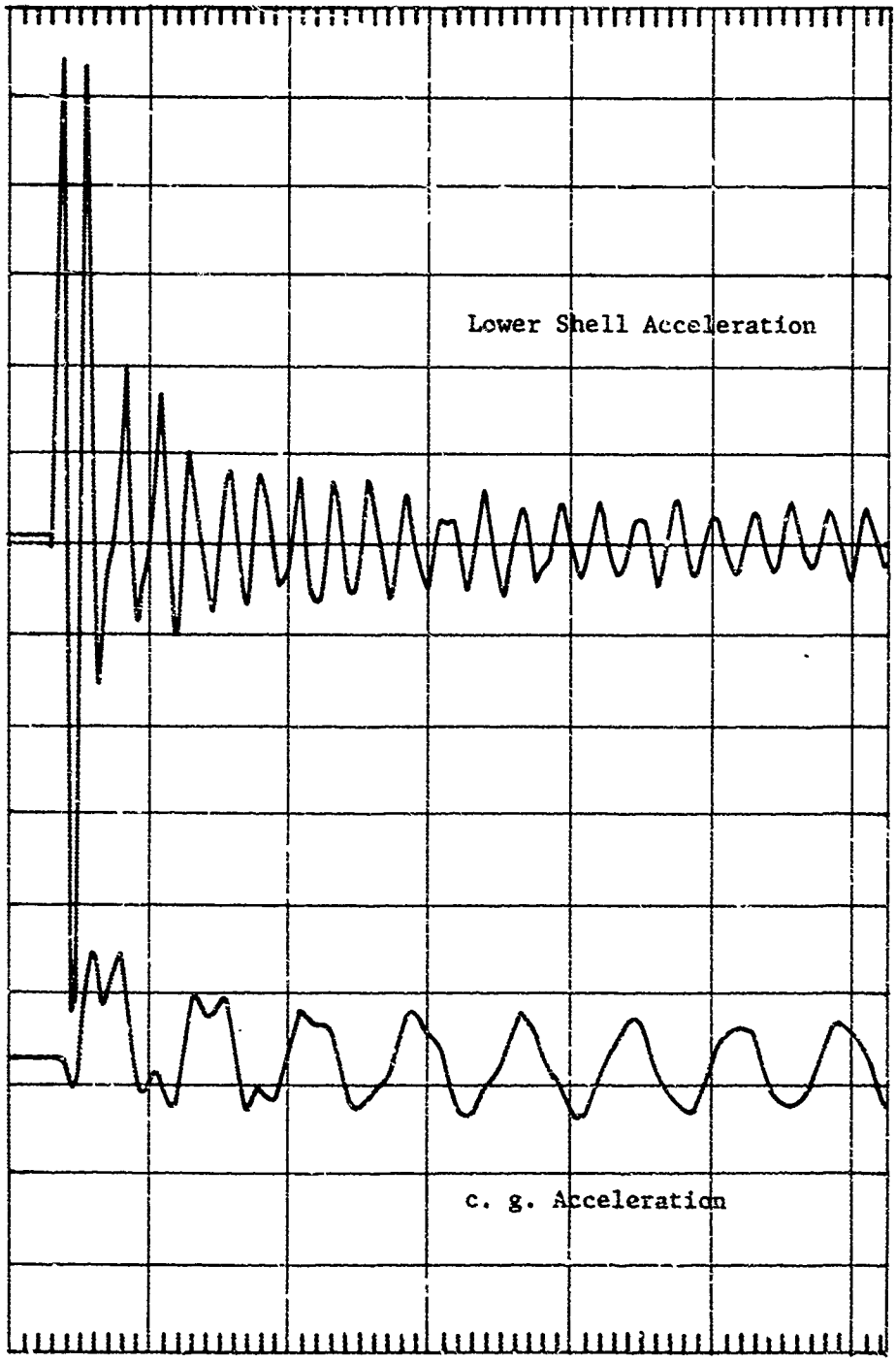

Figure 33

Tracing of Acceleration Record for Model with 0.080 Inch Thick Shell

Table XI

Experimental Results for Model with 0.032 Inch Thick Shell

Drop No.	Trace No.	Frequency (cps)	Film Amplitude (in)	Acceleration (Peak g)	Remarks
4	2 (shell)	700-750	±0.48	38.4	High damping. Component decayed in 0.08 sec.
		276 (average)	±2.625	210	System became saturated (overloaded) at the amplitude indicated. This component (frequency) continued to oscillate at lower g levels for a long period (extremely low damping).
	3 (c.g.)	700-750	±0.10	8.0	High damping
		276	(very low)	-	
		115 (average)	±0.28	22.4	g level near impact
		115	±0.50	40.0	g level at 0.03 sec after impact
		115	±0.40	32.0	g level at 0.10 sec after impact Long time oscillations (very low damping)
		Transient impact pulse period 0.01-0.02 sec.	+0.26	20.8	Estimated rise time; 0.002-0.003 sec.

Table XII

Experimental Results for Model with 0.050 Inch Thick Shell

Drop No.	Trace No.	Frequency (cps)	Film Amplitude (in)	Acceleration (Peak g)	Remarks
5	2 (shell)	330 (average)	±2.625	210.	System was overloaded for first few cycles. Frequency indicated applies to the first six cycles
		352 (average)	-	-	Frequency over second six cycles
		285 (average)	-	-	Frequency over third six cycles. There appears to be two closely spaced frequencies. Damping is very low after approximately 0.05 seconds.
	3 (c.g.)	330 (average)	±0.21	16.8	High damping. Component decayed appreciably after 0.05 seconds.
		120 (average)	± .31	24.8	Amplitude immediately following impact
		120 (average)	± .18	14.4	Amplitude after 0.20 seconds (very low damping)
		Transient impact pulse period 0.01-0.02 sec.	+0.22	17.6	Estimated time to rise: 0.002 - 0.003 seconds.

Table XIII

Experimental Results for Model with 0.080 Inch Thick Shell

Drop No.	Trace No.	Frequency (cps)	Film Amplitude (in)	Acceleration (Peak g)	Remarks
6	2 (shell	400 (average)	±2.625	210.	Amplitude decayed to ±0.35 inches in .015 sec. System was overloaded at first. Frequency indicated is average over first six cycles.
		425	-	-	Frequency over second six cycles.
		332	-	-	Frequency after 0.10 seconds. (very low damping)
	3 (c.g.)	400 (average)	±0.15	12.0	High damping
		133	±0.30	24.0	Amplitude immediately following impact
		133	±0.16	12.8	Amplitude after 0.2 seconds (very low damping)
		Transient impact pulse period 0.01 - 0.02 sec.	+0.20	16.0	Estimated time to rise: 0.002 - 0.003 seconds.

Appendix D

Instrumentation Characteristics

1. Endevco Model 2245B Accelerometers
   - Sensing element - piezoelectric
   - Resonant frequency - 28 KC or higher
   - Frequency response - flat within 5% to 5 KC
   - Amplitude linearity - Within ± 2% up to ± 1000g
   - Sensitivity - Approximately 2.25 rms mv per peak g with 30 feet of accelerometer cable

2. Modified Endevco Model 2607 Amplifiers
   - Gain - Continuously adjustable from 5 to 500 or greater
   - Maximum output voltage - Approximately 5 volts rms
   - Input impedance - Nominally 1000 megohms
   - Output impedance - 50 ohms in series with 4 microfarad capacitor
   - Amplitude linearity - within ± 1%

3. Spencer-Kennedy Model 302 Electronic Filters
   - Pass band - continuously adjustable in both bandwidth and frequency in 20 cps to 200 KC range
   - Insertion loss - 0 ± 1 db
   - Maximum input voltage - 6 volts peak
   - Input impedance - 2 megohms
   - Attenuation - 3.5 db at cutoff frequencies and 36 db per octave in rejection band
   - Output impedance - 300 ohms

4. Type 531 Textronix Oscilloscope with Type 53 GA Plug-in Unit
   - Type input - Differential (DC or AC)
   - Input impedance - 1 megohm
   - Maximum input voltage - 40 volts peak on 1 volt/cm range
     - 80 volts peak on 2 volt/cm range
   - Frequency response - flat within 3 db from 0 to 15 mc
   - Output - Vertical-output terminal where voltage proportional to input A, imput B, or A-B may be obtained

5. Bruel & Kjaer Vibration Pickup Amplifier and Frequency Analyzer
   - Function - Performs double integration
   - Selected frequency range - 30 cps and above
   - Maximum input with gain settings used - 2.5 volts rms at 100 cps

6. Honeywell Model T6GA-500 Galvonometer Amplifier
   - Gain - 0-1, continuously variable
   - Maximum output - 65 ma into 37 ohm load

7. Honeywell M5000 Galvanometers
   Sensitivity - 31.3 ma/inch or 1.23 volts/inch

8. Honeywell Model 1012 Direct Writing Recorder
   Paper speed - adjustable from .1 to 160 in/sec
   Timing lines - 1, 10, 100 & 1000 lines/sec

9. Lockheed Electronics Model 417C Tape Recorder

10. International Telephone and Telegraph Co. (Industrial Products Division) Model CS-101 Accelerometer Calibration System

Vita

Ralph N. Bingman was born on 1 June 1926 in St. Louis, Missouri, the son of Norbert M. Bingman and Minnie S. Bingman. After graduating from Carmi High School, Carmi, Illinois, in 1944, he entered the U. S. Army and served as an infantryman in the South Pacific Theater. He entered the University of Illinois in January 1947 and received an Aeronautical Engineer's degree in January 1951. He is a member of Tau Beta Pi, Phi Eta Sigma and Sigma Tau.

He is employed by the Vehicle Dynamics Division (FDDS), Air Force Flight Dynamics Laboratory, Wright-Patterson AFB, Ohio.

This thesis was typed by Mrs. Zelta Fogt.

Unclassified

Security Classification

DOCUMENT CONTROL DATA - R & D

(Security classification of title, body of abstract and indexing annotation must be entered when the overall report is classified)

1. ORIGINATING ACTIVITY *(Corporate author)* Air Force Insititute of Technology Wright-Patterson AFB Ohio	2a. REPORT SECURITY CLASSIFICATION Unclassified 2b. GROUP

3. REPORT TITLE

4. DESCRIPTIVE NOTES *(Type of report and inclusive dates)*
Thesis

5. AUTHOR(S) *(First name, middle initial, last name)*
Ralph N. Bingman

6. REPORT DATE June 1967	7a. TOTAL NO. OF PAGES 114	7b. NO. OF REFS
8a. CONTRACT OR GRANT NO. b. PROJECT NO. c. d.	9a. ORIGINATOR'S REPORT NUMBER(S) GAM/MECH 67-1 9b. OTHER REPORT NO(S) *(Any other numbers that may be assigned this report)*	

10. DISTRIBUTION STATEMENT
This document is subject to special export controls and each transmittal to foreign governments or foreign nationals may be made only with prior approval of the Dean, School of Engineering, Air Force Institute of Technology (AFIT-SE), Wright-Patterson Air Force Base, Ohio 45433.

11. SUPPLEMENTARY NOTES	12. SPONSORING MILITARY ACTIVITY

13. ABSTRACT

Theoretical and experimental investigations were made of responses of spherical shell structures subjected to water impact loads. Effects of structural flexibility were evaluated and a simple mathematical model for predicting dynamic loads in a spherically shaped structure was developed. Six model tests were conducted; qualitative agreement was obtained between the theoretical and experimental results. Theroretically predicted coupled responses of the model and water were observed in the test results. The theoretically predicted response frequencies averaged 20 percent above the measured frequencies. Predicted acceleration levels averaged 10 percent lower than the experimentally determined values.

DD FORM 1 NOV 65 1473

Security Classification

Security Classification

14. KEY WORDS	LINK A		LINK B		LINK C	
	ROLE	WT	ROLE	WT	ROLE	WT

Security Classification